Article

Cell Reports

The NAD+ Precursor Nicotinamide Riboside Rescues Mitochondrial Defects and Neuronal Loss in iPSC and Fly Models of Parkinson's Disease

Graphical Abstract

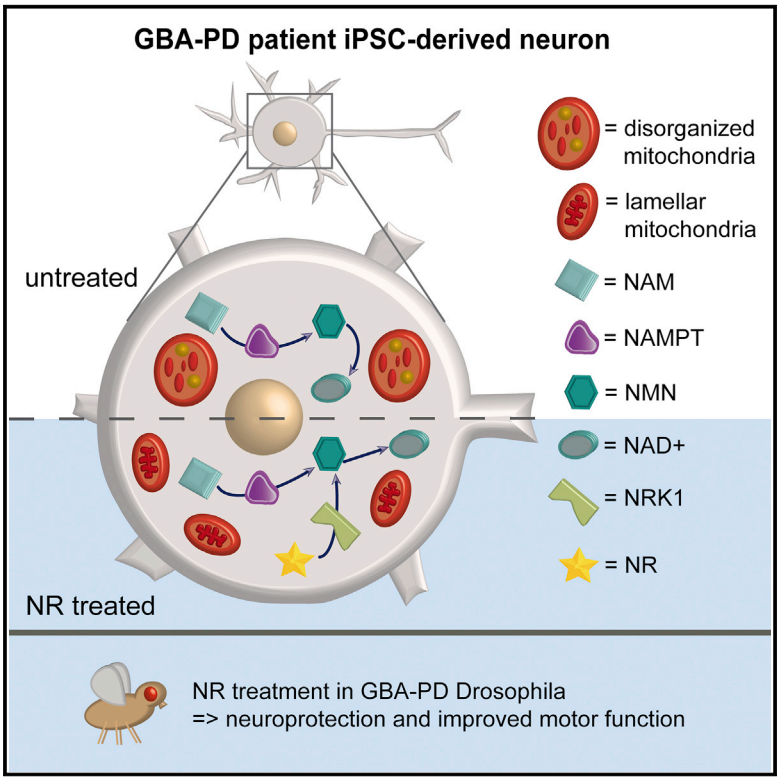

Highlights

- NAD+ metabolism and mitochondrial function are altered in GBA-PD neurons
- Human iPSC-derived neurons are responsive to NAD+ precursors
- Nicotinamide riboside improves mitochondrial function in GBA-PD iPSC neurons
- Nicotinamide riboside rescues neuronal loss and motor deficits in GBA-PD flies

Authors

David C. Schöndorf, Dina Ivanyuk, Pascale Baden, ..., Thomas Gasser, Alexander J. Whitworth, Michela Deleidi

Correspondence

michela.deleidi@dzne.de

In Brief

Mitochondrial damage is a key feature in Parkinson's disease. Schöndorf et al. demonstrate that nicotinamide riboside, an NAD+ precursor, boosts mitochondrial function in neurons derived from Parkinson's disease patient stem cells and is neuroprotective in Parkinson's disease fly models. These findings support use of NAD+ precursors in Parkinson's and other neurodegenerative diseases.

Schöndorf et al., 2018, Cell Reports *23*, 2976–2988
June 5, 2018 © 2018 The Authors.
https://doi.org/10.1016/j.celrep.2018.05.009

CellPress

OPEN ACCESS
CellPress

Cell Reports
Article

The NAD+ Precursor Nicotinamide Riboside Rescues Mitochondrial Defects and Neuronal Loss in iPSC and Fly Models of Parkinson's Disease

David C. Schöndorf,[1,2] Dina Ivanyuk,[1,2,8] Pascale Baden,[1,2,8] Alvaro Sanchez-Martinez,[3] Silvia De Cicco,[1,2] Cong Yu,[1,2] Ivana Giunta,[3] Lukas K. Schwarz,[1,2] Gabriele Di Napoli,[1,2] Vasiliki Panagiotakopoulou,[1,2] Sigrun Nestel,[4] Marcus Keatinge,[5] Jan Pruszak,[6,7] Oliver Bandmann,[5] Bernd Heimrich,[4] Thomas Gasser,[1,2] Alexander J. Whitworth,[3] and Michela Deleidi[1,2,9,*]

[1]German Center for Neurodegenerative Diseases (DZNE), Helmholtz Association, Tübingen 72076, Germany
[2]Hertie-Institute for Clinical Brain Research, University of Tübingen, Tübingen 72076, Germany
[3]Medical Research Council Mitochondrial Biology Unit, University of Cambridge, Cambridge Biomedical Campus, Hills Road, Cambridge CB2 0XY, UK
[4]Department of Neuroanatomy, Institute of Anatomy and Cell Biology, University of Freiburg, Freiburg 79104, Germany
[5]Sheffield Institute for Translational Neuroscience (SITraN), University of Sheffield, Sheffield, UK
[6]Emmy Noether-Group for Stem Cell Biology, Department of Molecular Embryology, Institute of Anatomy and Cell Biology, Faculty of Medicine, University of Freiburg, Freiburg, Germany
[7]Center for Biological Signaling Studies (BIOSS), University of Freiburg, Freiburg 79104, Germany
[8]These authors contributed equally
[9]Lead Contact
*Correspondence: michela.deleidi@dzne.de
https://doi.org/10.1016/j.celrep.2018.05.009

SUMMARY

While mitochondrial dysfunction is emerging as key in Parkinson's disease (PD), a central question remains whether mitochondria are actual disease drivers and whether boosting mitochondrial biogenesis and function ameliorates pathology. We address these questions using patient-derived induced pluripotent stem cells and *Drosophila* models of *GBA*-related PD (*GBA*-PD), the most common PD genetic risk. Patient neurons display stress responses, mitochondrial demise, and changes in NAD+ metabolism. NAD+ precursors have been proposed to ameliorate age-related metabolic decline and disease. We report that increasing NAD+ via the NAD+ precursor nicotinamide riboside (NR) significantly ameliorates mitochondrial function in patient neurons. Human neurons require nicotinamide phosphoribosyltransferase (NAMPT) to maintain the NAD+ pool and utilize NRK1 to synthesize NAD+ from NAD+ precursors. Remarkably, NR prevents the age-related dopaminergic neuronal loss and motor decline in fly models of *GBA*-PD. Our findings suggest NR as a viable clinical avenue for neuroprotection in PD and other neurodegenerative diseases.

INTRODUCTION

Mitochondrial dysfunction has been proposed as a key mechanism in many neurodegenerative diseases. Among others, Parkinson's disease (PD) stands out due to the role of PD-linked genes in mitochondrial function and dynamics (Exner et al., 2012). Evidence for mitochondrial dysfunction in PD was first described in the 1980s by Schapira et al., who showed complex I (CI) defects in cells and tissues from PD patients (Schapira et al., 1989). Substantial progress has been made since, and genetic and biochemical studies now indicate that mitochondrial dysfunction and cellular energy failure are key to PD (Jansen et al., 2017). In this respect, recent studies have shown that the activation of pathways related to mitochondrial biogenesis and energy metabolism, such as the NAD+/sirtuin 1 (SIRT1) pathway, provides protection against aging-related disease (Rajman et al., 2018). Similar approaches could be easily translated into treatment for PD. However, it is still unclear whether mitochondrial defects are actual disease drivers and increasing mitochondrial biogenesis provides neuroprotection in PD. In addition, little is known about NAD+ metabolism and availability of NAD+ precursors in human neurons. Here, we have addressed these fundamental questions in an induced pluripotent stem cell (iPSC) neuronal model of PD bearing mutations in the lysosomal enzyme β-Glucocerebrosidase (*GBA*) gene (*GBA*-PD), the most common genetic risk for PD (Sidransky et al., 2009). β-Glucocerebrosidase (GCase) activity is reduced not only in mutation carriers but also in idiopathic PD and healthy individuals at older age (Gegg et al., 2012; Rocha et al., 2015), pointing toward a general role for GCase in brain aging and neurodegenerative processes. Importantly, patients with *GBA* mutations represent an etiologically homogeneous subgroup of PD, therefore providing the ideal cohort for precision medicine approaches.

The pathogenetic mechanisms involved in *GBA*-PD are only partially understood and include autophagic defects, increased α-synuclein aggregation, calcium dyshomeostasis,

This is an open access article under the CC BY license (http://creativecommons.org/licenses/by/4.0/).

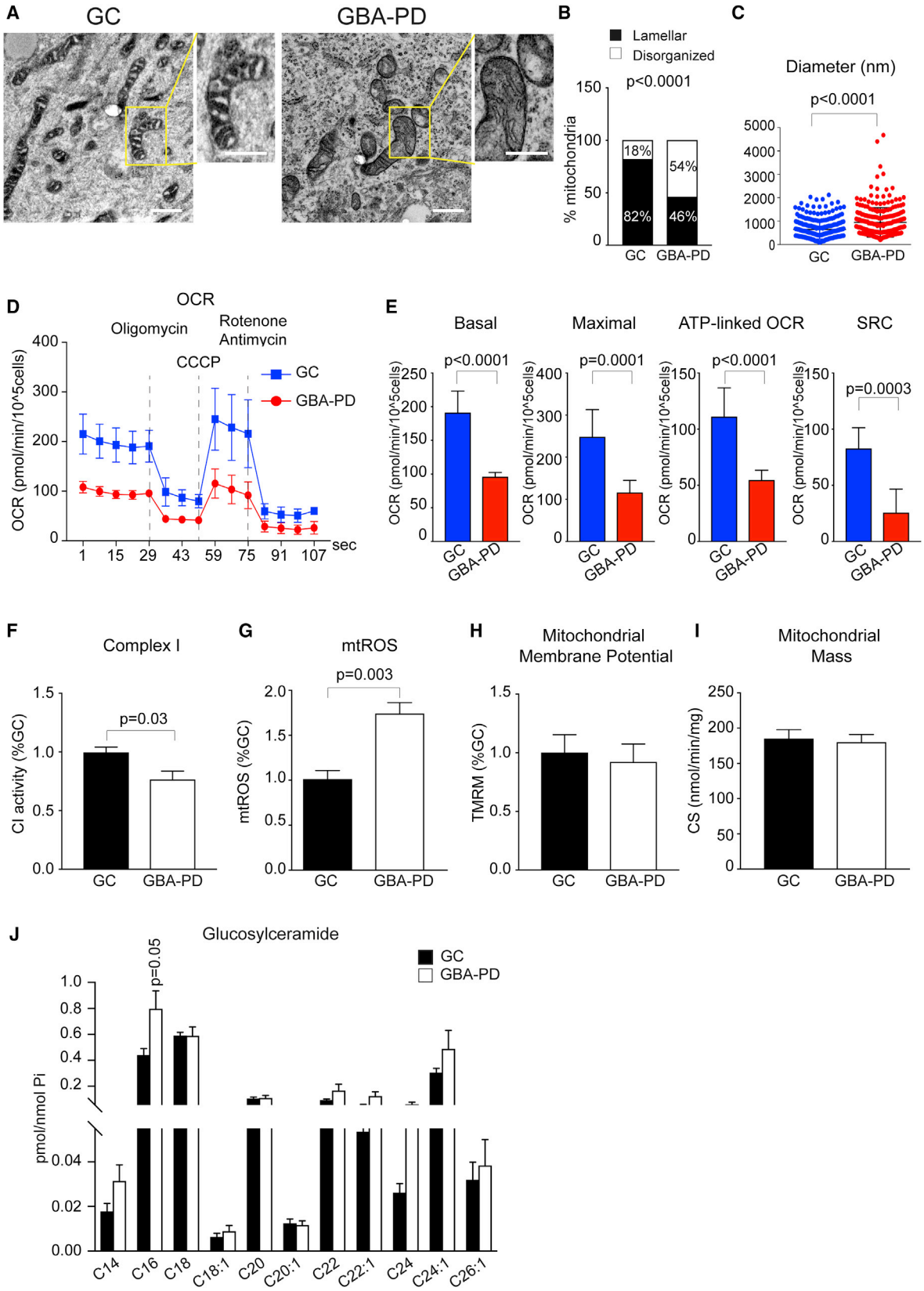

(legend on next page)

and endoplasmic reticulum (ER) stress (Migdalska-Richards and Schapira, 2016). GCase is a lysosomal enzyme that catalyzes the hydrolysis of glucosylceramide (GlcCer), a membrane glycosphingolipid, to ceramide and glucose, and both loss and gain of its enzymatic function may contribute to disease. According to the loss-of-function hypothesis, GCase deficiency causes substrate accumulation that alters lysosomal function and promotes α-synuclein aggregation (Jo et al., 2000; Velayati et al., 2010; Mazzulli et al., 2011). GCase is glycosylated and folded in the ER and subsequently trafficked through the Golgi to the lysosome. According to the gain-of-function hypothesis, *GBA* mutations interfere with the folding process in the ER, leading to ER-associated degradation, ER stress, and activation of the unfolded protein response (UPR) (Maor et al., 2013; Fernandes et al., 2016). Interestingly, mitochondrial dysfunction has been described in experimental models of GCase deficiency (Osellame et al., 2013; Keatinge et al., 2015; Cleeter et al., 2013). However, whether mitochondrial function is altered in PD patients with *GBA* mutations (*GBA*-PD) and the mechanisms underlying such demise are still unknown. Furthermore, whether improving mitochondrial biogenesis and function represents an effective therapeutic strategy for PD needs to be investigated.

RESULTS

iPSC-Derived Neurons from *GBA*-PD Patients Show Defects in Mitochondrial Function

To investigate whether *GBA* is linked to mitochondrial function in human neurons, iPSC lines from PD patients with heterozygous *GBA* mutations (N370S, L444P, and RecNcil), as well as corresponding isogenic gene-corrected (GC) and unaffected controls (Schöndorf et al., 2014) (Table S1), were differentiated into dopaminergic (DA) neurons, and mitochondrial morphology was examined by transmission electron microscopy (TEM). Morphometric analysis revealed altered cristae morphology in *GBA*-PD neurons compared to isogenic GC and healthy controls (Figures 1A, 1B, and S1A). In addition, *GBA*-PD neurons showed a significant increase in mitochondrial diameter (Figure 1C). Next, we measured oxygen consumption rates (OCRs) and found that *GBA*-PD neurons displayed significantly reduced basal respiration and decreased maximal OCR as well as ATP-linked OCR and spare respiratory capacity (SRC) compared to isogenic controls (Figures 1D and 1E). Similarly, basal respiration, maximal OCR, and ATP-linked OCR and SRC were significantly reduced in *GBA*-PD neurons compared to unrelated unaffected controls (Figure S1B). Western blot analysis revealed an increase in the level of respiratory chain complex subunits in *GBA*-PD neurons compared to isogenic controls, but this increase did not reach statistical significance (Figures S1C and S1D). We next measured CI activity in enriched mitochondrial fractions from *GBA*-PD iPSC neurons and GC controls. CI activity was significantly reduced in *GBA*-PD neurons compared to isogenic controls (Figure 1F). Consistent with these findings, *GBA*-PD neurons produced significantly higher amounts of mitochondrial reactive oxygen species (mtROS) than isogenic controls (Figure 1G). However, mitochondrial membrane potential and mitochondrial mass were not significantly changed in *GBA*-PD neurons (Figures 1H and 1I). Of note, no significant difference in the degree of mitochondrial function was observed among different *GBA* genotypes, suggesting that the genotypes examined in this study (RecNcil, L444P, and N370S) equally affect mitochondria (Figures S1E–S1I). To get further insight into the mechanisms underlying mitochondrial dysfunction in *GBA*-PD, we examined the GCase substrate sphingolipid composition of mitochondria from *GBA*-PD neurons and isogenic controls by high-performance liquid chromatography tandem mass spectrometry (HPLC-MS/MS). To this end, mitochondria were isolated from iPSC neurons with a high degree of purity. Western blot analysis showed high level of enrichment of isolated mitochondria with a small amount of non-mitochondrial organelle contamination (Figure S1J). Quantification of individual species of GlcCer revealed the absence of GlcCer accumulation in patient mitochondria with only a significant increase of C16-GlcCer (Figure 1J).

iPSC-Derived Neurons from *GBA*-PD Patients Show Defects in Mitochondrial Dynamics

Next, we examined the level of mitochondrial fission (DRP1 and Fis1) and fusion (OPA1 and Mfn1) proteins in *GBA*-PD iPSC neurons and isogenic controls. Immunoblot analysis revealed a

Figure 1. Mitochondrial Function in *GBA*-PD iPSC Neurons

(A–C) Mitochondrial morphology in isogenic gene-corrected (GC) controls and *GBA*-PD iPSC neurons.

(A) Representative TEM images of mitochondria are shown (L444P *GBA*-PD and GC controls) (scale bar, 500 nm).

(B) Quantification of mitochondrial cristae morphology in isogenic GC and *GBA*-PD (N370S, L444P) iPSC-derived neurons (n = 3; two-sided Fisher's exact test).

(C) Mitochondrial major diameter. Data are presented as mean ± SD (n = 299 GC and n = 264 *GBA*-PD mitochondria from 3 independent experiments were analyzed; two-tailed t test).

(D) Oxygen consumption rate (OCR) trace for isogenic GC and *GBA*-PD (N370S, L444P, RecNcil) iPSC neurons. Data are normalized to cell number and presented as mean ± SD (n = 8; two-tailed t test).

(E) Quantification of basal, maximal, ATP-linked respiration, and spare respiratory capacity (SRC). Data are normalized to cell number and presented as mean + SD (n = 8; two-tailed t test).

(F) Complex I (CI) activity in enriched mitochondria from isogenic *GBA*-PD (N370S, L444P) and GC iPSC neurons. Data are expressed as mean + SEM (n = 5; two-tailed t test).

(G) Mitochondrial ROS (mtROS) levels in *GBA*-PD (N370S, L444P, RecNcil) and GC iPSC neurons. Data are normalized to GC and represented as mean + SEM (n = 5; two-tailed t test).

(H) Mitochondrial membrane potential in isogenic GC and *GBA*-PD (N370S, L444P, RecNcil) iPSC neurons. Data are normalized to GC and presented as mean + SEM (n = 5; two-tailed t test).

(I) Citrate synthase (CS) activities in GC and *GBA*-PD (N370S, L444P, RecNcil) iPSC neurons. Data are presented as mean + SEM (n = 5; two-tailed t test).

(J) Mitochondrial sphingolipid profile of isogenic GC and *GBA*-PD (N370S, L444P) iPSC neurons. Data are normalized to inorganic phosphate (Pi) and presented as mean + SEM (n = 7 independent mitochondrial purifications; two-tailed t test).

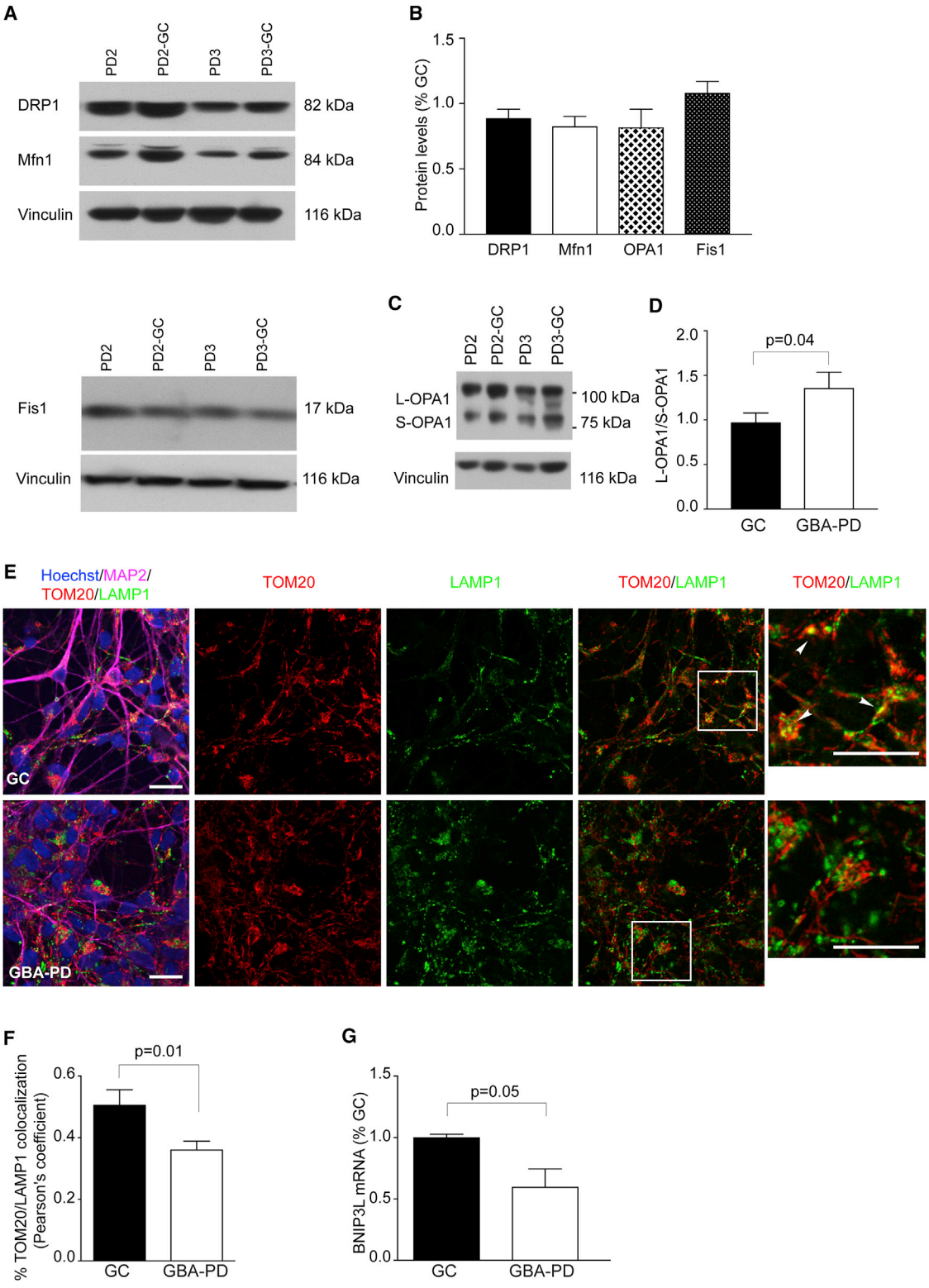

Figure 2. Mitochondrial Dynamics in *GBA*-PD iPSC Neurons

(A and B) Western blot of DRP1, Mfn1, and Fis1 in isogenic *GBA*-PD (N370S, L444P) and gene-corrected (GC) iPSC neurons (A). Vinculin was used as a loading control. Quantification of western blots is shown in (B). Data are normalized to GC and presented as mean + SEM (n = 5).

(C and D) Western blot analysis of OPA-1 processing (C). The L-OPA1/S-OPA-1 ratio is shown in (D). Data are presented as mean + SEM (n = 5; two-tailed t test).

(legend continued on next page)

reduction in DRP1, OPA1, and Mfn1 levels in *GBA*-PD neurons (Figures 2A–2D). On the other hand, there was an increase of Fis1 in *GBA*-PD neurons (Figures 2A and 2B). However, these differences did not reach statistical significance. Interestingly, the ratio between the long and short form of OPA1 was significantly increased in *GBA*-PD neurons compared to isogenic controls, suggesting an impairment of mitophagy (MacVicar and Lane, 2014) (Figures 2C and 2D). *GBA*-PD neurons showed a significant reduction of mitochondrial-lysosomal co-localization compared to GC controls, as assessed by confocal microscopy and Amnis ImageStream flow cytometry (Figures 2E, 2F, S2A, and S2B). In line with these findings, the expression of the mitophagy adaptor protein BNIP3L/NIX was significantly reduced in *GBA*-PD compared to isogenic controls (Figure 2G).

Mitochondrial Function Is Altered in *GBA* Knockout iPSC-Derived Neurons

To assess the impact of loss of GCase enzymatic function on mitochondria in the absence of gain-of-function mechanisms, we generated *GBA* knockout (KO) iPSCs using clustered regularly interspaced short palindromic repeats (CRISPR)-Cas9 (Figures S3A–S3F). *GBA* was knocked out in two healthy control iPSC lines and one *GBA-PD* N370S iPSC line (Table S2). All *GBA* KO clones showed complete loss of GCase protein and its enzymatic activity (Figures S3E and S3F). No significant difference in DA neuronal differentiation potential was observed among *GBA* KO iPSCs and corresponding parental lines as assessed by quantification of βIII-tubulin- and tyrosine hydroxylase (TH)-positive neurons (>80% neurons, of which on average 40% of cells in both controls and *GBA* KO lines expressed TH). *GBA* KO iPSC-derived neurons exhibited accumulation of the GCase substrates GlcCer and glucosylsphingosine as revealed by HPLC-MS/MS (Figures S3G). A significant increase of C16-galactosylceramide was also observed (Figure S3I). No significant change in levels of other sphingolipids was detected (Figures S3H and S3I). Two *GBA* KO clones were selected from each parental iPSC line and used for further experiments (Table S2). As observed in *GBA*-PD neurons, morphometric analysis revealed ultrastructural abnormalities in *GBA* KO iPSC-neurons compared to isogenic controls (Figures 3A and 3B). Similar to what we observed in *GBA*-PD neurons, *GBA* KO neurons showed significantly reduced basal and maximal respiration as well as ATP-linked OCR and SRC (Figure 3C). Despite the consistent trend for decreased CI activity in *GBA* KO neurons, the values did not reach statistical significance (Figure 3D). *GBA* KO neurons showed elevated levels of mtROS (Figure 3E). Furthermore, we did not observe significant changes of mitochondrial membrane potential (Figure 3F). HPLC-MS/MS analysis of mitochondria purified from *GBA* KO iPSC-derived neurons showed a significant accumulation of all subtypes of the GCase substrates GlcCer and glucosylsphingosine (Figure 3G).

GBA-PD, but Not *GBA* Knockout, iPSC-Derived Neurons Show Increased ER Stress and UPR

Interestingly, when comparing OCRs and CI activity in the isogenic lines (*GBA*-PD N370S, GC control and *GBA* KO), no gene dosage effect was found (Figures S3J and S3K). These data suggest that different mechanisms contribute to mitochondrial defects in heterozygous *GBA*-PD patient and *GBA* KO neurons. One of such mechanisms could be the UPR and ER stress that have been previously observed in *GBA-PD* (Fernandes et al., 2016). To dissect the contribution of gain- and loss-of-function of mutant GCase, we measured the levels of the ER chaperone immunoglobulin-binding protein (BiP) by western blot in *GBA*-PD N370S iPSC-derived neurons as well as isogenic controls and isogenic *GBA* KO neurons. Levels of BiP were increased in *GBA*-PD neurons compared to isogenic controls and isogenic *GBA* KO neurons (Figure 4A). Consistent with these findings, RNA levels of spliced X-box-binding protein-1 (XBP1s) were significantly increased in *GBA*-PD, but not in isogenic *GBA* KO neurons, suggesting activation of the IRE1 related branch of ER stress (Figure 4B). Healthy control-derived *GBA* KO neurons showed levels of BiP similar to their isogenic controls (Figure S3L). In addition, levels of phospho-eIF2α were significantly increased in *GBA*-PD, but not in isogenic *GBA* KO neurons, as compared to GC controls (Figure 4C). Consistent with these findings, levels of phospho-PERK were increased only in *GBA*-PD neurons as compared to GC controls (Figure 4D).

NAD+ Metabolism Is Altered in *GBA*-PD iPSC-Derived Neurons

Mitochondrial dysfunction and increased oxidative stress are hallmarks of aging and have been linked to the decline of intracellular levels of NAD+ (Mouchiroud et al., 2013). To examine whether *GBA* mutations lead to changes in NAD+ metabolism, we measured the expression of the NAD+ biosynthetic enzymes nicotinamide mononucleotide adenylyltransferases (NMNATs). mRNA levels of NMNAT2 were significantly decreased in *GBA*-PD neurons compared to isogenic controls, whereas levels of NMNAT1 and NMNAT3 were unchanged (Figure 5A). NMNAT2 levels were unchanged in *GBA* KO neurons (Figure S3M). Levels of nicotinamide phosphoribosyltransferase (NAMPT), the rate-limiting enzyme in the NAD+ salvage synthesis pathway, were similar in both groups (*GBA*-PD and GC controls), as assessed by qRT-PCR (Figure 5A). Next, we measured the adenine and pyridine nucleotide pool in *GBA*-PD and isogenic control as well as *GBA* KO iPSC-neurons by targeted metabolomics using liquid chromatography-mass spectrometry (LC-MS). The intracellular NAD+ content was maintained in *GBA*-PD and *GBA* KO neurons (Figure S4). To exclude that the observed absence of significant changes of NAD+ levels could be linked to the absence of overt neurodegeneration in our stem cell-based model system, we also examined the NAD+ metabolome in adult *gba*$^{+/+}$, *gba*$^{-/-}$, and gba$^{+/-}$ whole zebrafish brains. Adult *gba*$^{-/-}$

(E) Immunostaining of differentiated iPSC cultures for MAP2 (magenta), TOM20 (red), and LAMP1 (green). Cell nuclei were counterstained with Hoechst (blue). Scale bar, 20 μm.

(F) Colocalization between LAMP1 and TOM20. Data are presented as mean + SEM (n = 5; two-tailed t test).

(G) BNIP3L mRNA levels in isogenic GC and *GBA*-PD (N370S, L444P) iPSC-derived neurons. Data are normalized on Rplp0 and OAZ1 and to GC and presented as mean + SEM (n = 5; two-tailed t test).

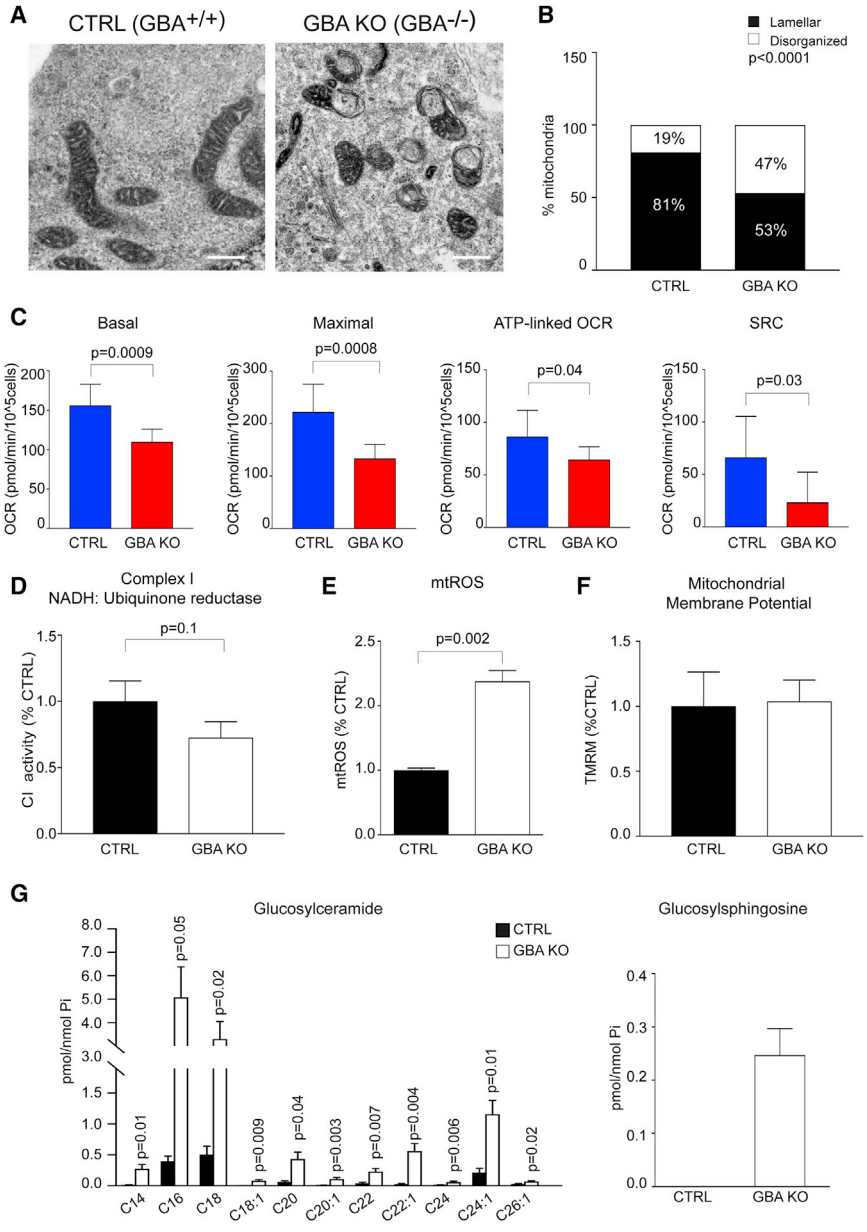

Figure 3. Mitochondrial Function in Human *GBA* KO iPSC Neurons

(A and B) Mitochondrial morphology in isogenic healthy control (CTRL) and *GBA* KO iPSC neurons. Representative TEM images of mitochondria (A; scale bar, 500 nm). Quantification of mitochondrial cristae morphology in isogenic CTRL and *GBA* KO iPSC-neurons (B). Data are presented as mean + SEM (n = 3; two-sided Fisher's exact test).

(C) Mitochondrial respiration. Data are presented as mean + SD (n = 5–7; two-tailed t test).

(D) CI activity in isogenic CTRL and *GBA* KO iPSC neurons. Data are expressed as mean + SEM (n = 5; two-tailed t test).

(E) mtROS levels normalized to CTRL and presented as mean + SEM (n = 5; two-tailed t test).

(F) Mitochondrial membrane potential. Data are presented as mean + SEM (n = 5; two-tailed t test).

(G) Mitochondrial sphingolipid profile of CTRL and *GBA* KO iPSC-neurons. GlcCer and glucosylsphingosine levels normalized by inorganic phosphate (Pi). Glucosylsphingosine was below detection limit in control mitochondria. Data are presented as mean + SEM (n = 4 independent mitochondrial purifications; two-tailed t test).

zebrafish recapitulate the key pathological aspects of PD, including DA neuronal loss, early microglial activation, and mitochondrial dysfunction (Keatinge et al., 2015). Metabolomic analyses revealed that the NAD+ pool was maintained in brains of adult *gba*$^{+/-}$ and *gba*$^{-/-}$ zebrafish (Figure S5). However, a significant increase in nicotinamide mononucleotide (NMN) was observed in *gba*$^{-/-}$ compared to *gba*$^{+/+}$ zebrafish brains as well as in *gba*$^{-/-}$ compared to *gba*$^{+/-}$ brains (Figure S5), suggesting an alteration of NAD+ metabolism. To rule out the possibility that the heterogeneity of the cell culture and whole brain tissues influences the results, we then employed the biosensor Peredox to monitor the cytosolic NADH/NAD+ ratio in single iPSC-derived neurons with live-cell imaging (Hung et al., 2011). The NAD+/NADH redox state was significantly reduced in *GBA*-PD iPSC neurons, suggesting reduced level of available NAD+ (Figure 5B). No significant change was observed in *GBA* KO neurons (Figure S3N).

The NAD+ Precursor Nicotinamide Riboside Rescues Mitochondrial Defects in *GBA*-PD iPSC-Derived Neurons

Next, we tested the ability of different NAD+ precursors to increase NAD+ levels in human iPSC-derived neurons. Control iPSC-derived neurons were treated with nicotinamide (NAM), NMN, or nicotinamide riboside (NR), and NAD+ levels were measured using a NAD+ cycling assay. NR and NMN showed the strongest effect in boosting NAD+ levels (Figure S6A). As NR represents a promising approach, as shown by pharmacokinetic studies in healthy subjects (Trammell et al., 2016), we investigated the ability of NR to rescue *GBA*-linked mitochondrial defects. NR significantly increased NAD+ and NADH levels in *GBA*-PD neurons (Figures S6B and S6C). NR treatment resulted in an increase in expression of markers of mitochondrial biogenesis (TFAM) and mitochondrial UPR (mtUPR) (HSP60) (Figure 5C). Consistent with these findings, mitochondrial DNA content and mitochondrial mass were increased after 48 hr in NR-treated samples (Figures 5D and 5E). The effect of NR was abrogated by EX527, a SIRT1-specific inhibitor, suggesting that SIRT1 is one of the mediators of NR function (Figure S6D). Importantly, NR restored mitochondrial cristae morphology and significantly reduced mtROS production in *GBA*-PD neurons (Figures 5F–5H). In parallel, NR

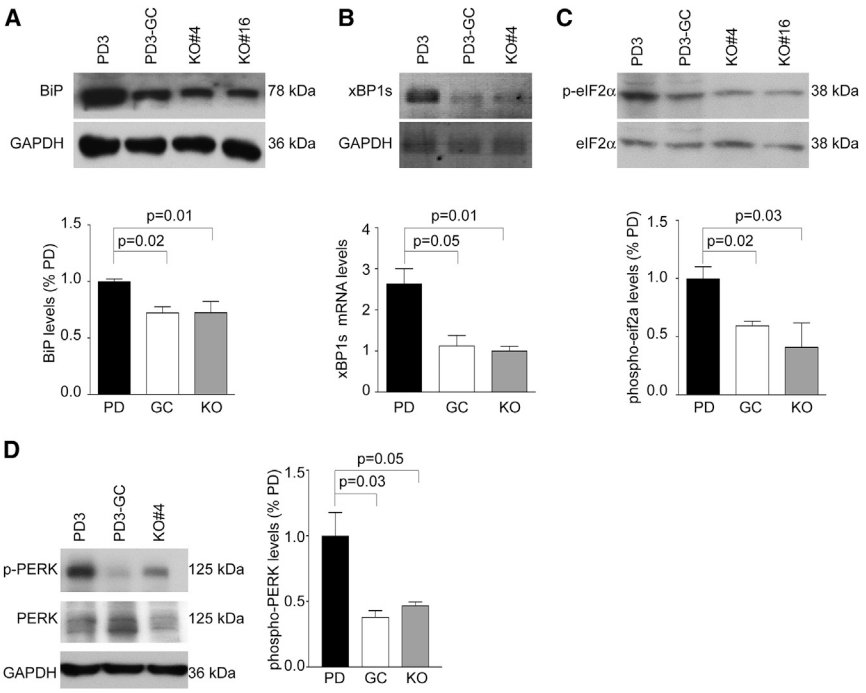

Figure 4. ER Stress Responses in *GBA*-PD and *GBA* KO iPSC Neurons

Analysis of ER stress responses and UPR was performed in isogenic *GBA*-PD (N370S), gene-corrected (GC) controls, and isogenic *GBA* KO (clones 4 and 16) iPSC neurons.

(A) Representative western blots showing BiP levels in isogenic *GBA*-PD, GC, and *GBA* KO iPSC neurons. BiP intensity bands were normalized to GAPDH and the corresponding isogenic control. Data are expressed as mean + SEM (n = 5; one-way ANOVA).

(B) Analysis of XBP1 splicing (XBP1s). mRNA levels of XBP1s were measured by qPCR. Representative agarose gel electrophoresis of qRT-PCR products is shown. For quantification, GAPDH served as reference gene. Data are expressed as mean + SEM (n = 5; one-way ANOVA).

(C) Representative western blots showing phospho-eIF2α/eIF2α levels in isogenic *GBA*-PD, GC, and *GBA* KO iPSC-derived neurons. For quantification, phospho-eIF2α intensity bands were normalized to total eif2α and the corresponding isogenic control. Data are expressed as mean + SEM (one-way ANOVA). Gel loading as in (A).

(D) Representative western blots showing phospho-PERK/PERK levels in isogenic *GBA*-PD, GC, and *GBA* KO iPSC-derived neurons. Data are expressed as mean + SEM (n = 5; one-way ANOVA).

treatment significantly reduced the mitochondrial membrane potential (Figure 5I). Similar results were observed when *GBA* KO neurons were treated with NR (Figures S6E–S6G). With regard to the observed defects in mitochondrial dynamics, NR altered the levels of mitochondrial shaping proteins, with a nonsignificant increase in DRP1, Mfn1, and OPA1 and a slight decrease in Fis1 (Figures 5J and 5K). The decreased levels of mitochondrial DNA content observed at 24 hr after NR treatment would suggest an increased mitochondrial clearance (Figure 5D). In line with these findings, NR was able to increase the levels of BNIP3L/NIX in *GBA*-PD neurons (Figure 5L). NR did not enhance mitochondrial respiration (Figures S6H and S6I). On the contrary, a significant decrease in basal respiration was observed in *GBA*-PD iPSC-derived neurons treated with NR (Figure S6H). In addition, NR treatment did not alter protein levels of BiP in *GBA*-PD neurons (Figure S6J). To confirm that increased NAD+ levels are responsible for the phenotypic rescue, we treated cells with the poly(ADP-ribose)-polymerase (PARP) inhibitor PJ34 that, differently from NAD+ precursors, increases NAD+ levels by inhibiting its consumption. Similar to NR, PJ34 significantly increased NAD+ levels in human-iPSC-derived neurons and rescued mitochondrial defects in *GBA*-PD neurons (Figures S7A–S7E). Taken together, these results suggest that increasing NAD+ levels rescues mitochondrial dysfunction via increased levels of NAD+ in patient-derived *GBA*-PD and *GBA* KO neurons.

Increasing NAD+ Improves Autophagy in *GBA*-PD and *GBA* KO Neurons

GBA mutations affect autophagy and lysosomal function, leading to autophagic block, defects in autophagosome clearance, and altered lysosomal recycling (Schöndorf et al., 2014; Magalhaes et al., 2016). To examine the effects of NR on autophagy, we treated *GBA*-PD and *GBA* KO neurons with NR and assessed parameters of autophagic function. NR treatment did not alter the levels of LC3II at basal conditions; however, it significantly increased LC3II levels in patient neurons treated with leupeptin and ammonium chloride, suggesting an increase of synthesis and clearance of autophagosomes (Figures S7F–S7I). The autophagic flux was significantly increased in *GBA* KO neurons and showed a nonsignificant increase in *GBA*-PD neurons after NR treatment (Figures S7F–S7I).

NR Metabolism and NAD+ Availability in Human iPSC-Derived Neurons

To examine pathways of NAD+ maintenance and NAD+ precursors utilization, control iPSC-derived neurons were treated with the NAMPT inhibitor FK866, and NAD+ levels were measured. FK866 treatment decreased intracellular NAD+ levels by more than 90% (Figure 6A). However, FK866 treatment did not alter the sensitivity of human neurons to NR treatment (Figure 6A), indicating that NR is metabolized into NAD+ in a NAMPT-independent pathway. We next measured the expression levels of the NAD+ biosynthesis enzymes NR kinase 1 and 2 (NRK1 and NRK2) (Bieganowski and Brenner, 2004). In undifferentiated iPSCs, NRK2 showed higher expression levels; on the contrary, levels of NRK1 were significantly higher in iPSC-derived neurons (Figure 6B). The role of NRKs in NAD+ metabolism in human neurons is still unknown. Given its high expression, we aimed to investigate whether NRK1 is essential for NR metabolism into NAD+ in human neurons. Of note, mRNA levels of NRK1 were not affected by NR treatment (Figure 6C). Next, we knocked down NRK1 in control iPSC-derived neurons using

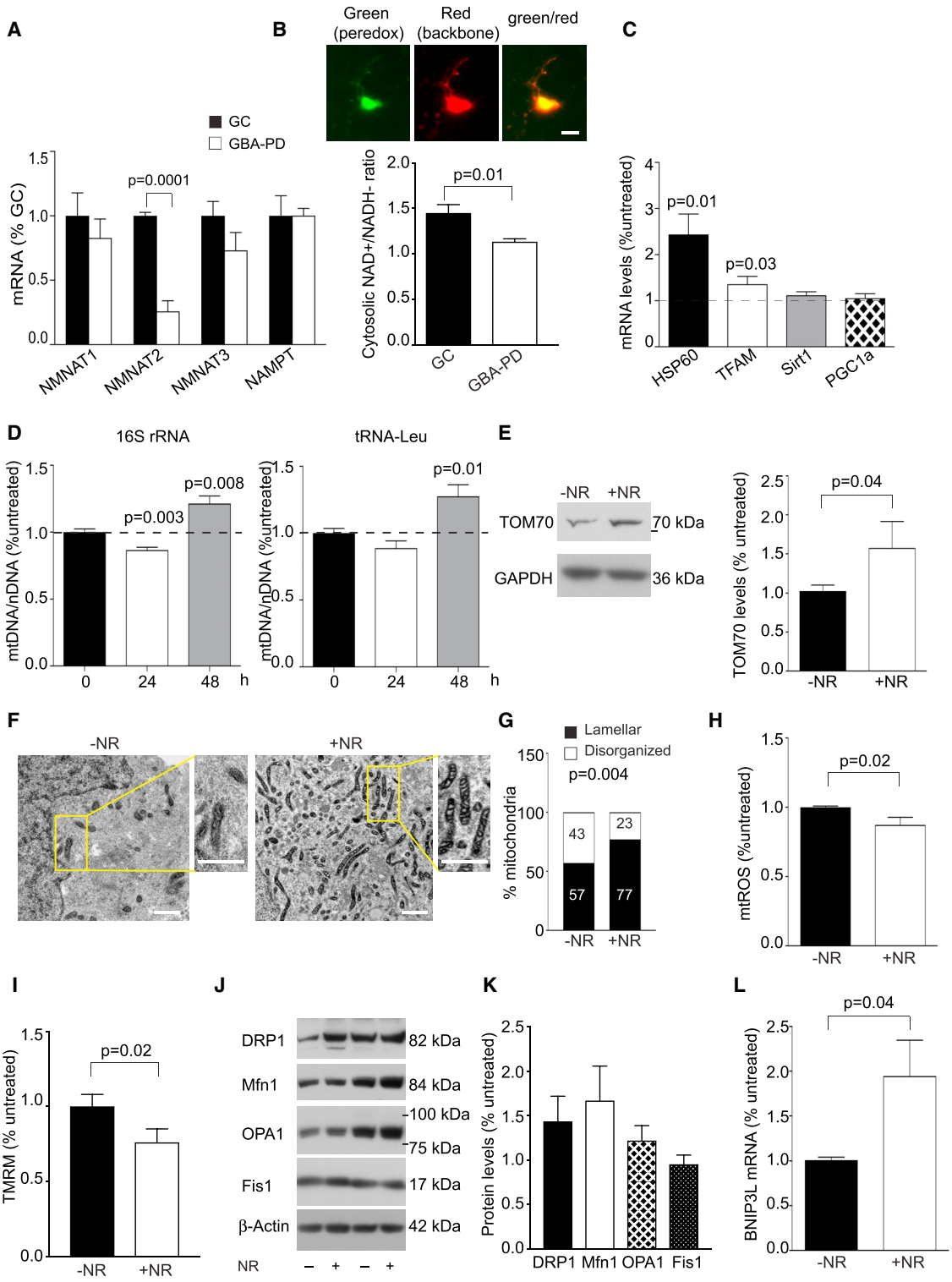

Figure 5. Nicotinamide Riboside Reverts Mitochondrial Defects in *GBA*-PD iPSC Neurons

(A) NMNAT1, NMNAT2, NMNAT3, and NAMPT mRNA levels in isogenic GC and *GBA*-PD (N370S, L444P) iPSC neurons. Data were normalized to the level of the housekeeping genes Rplp0 and OAZ and expressed as fold change over PD. Data are expressed as mean + SEM (n = 5; two-tailed t test).

(B) The NAD+/NADH redox state was measured in iPSC-derived neurons using the biosensor Peredox. Results are presented as mean + SEM (n = 5; two-tailed t test).

(legend continued on next page)

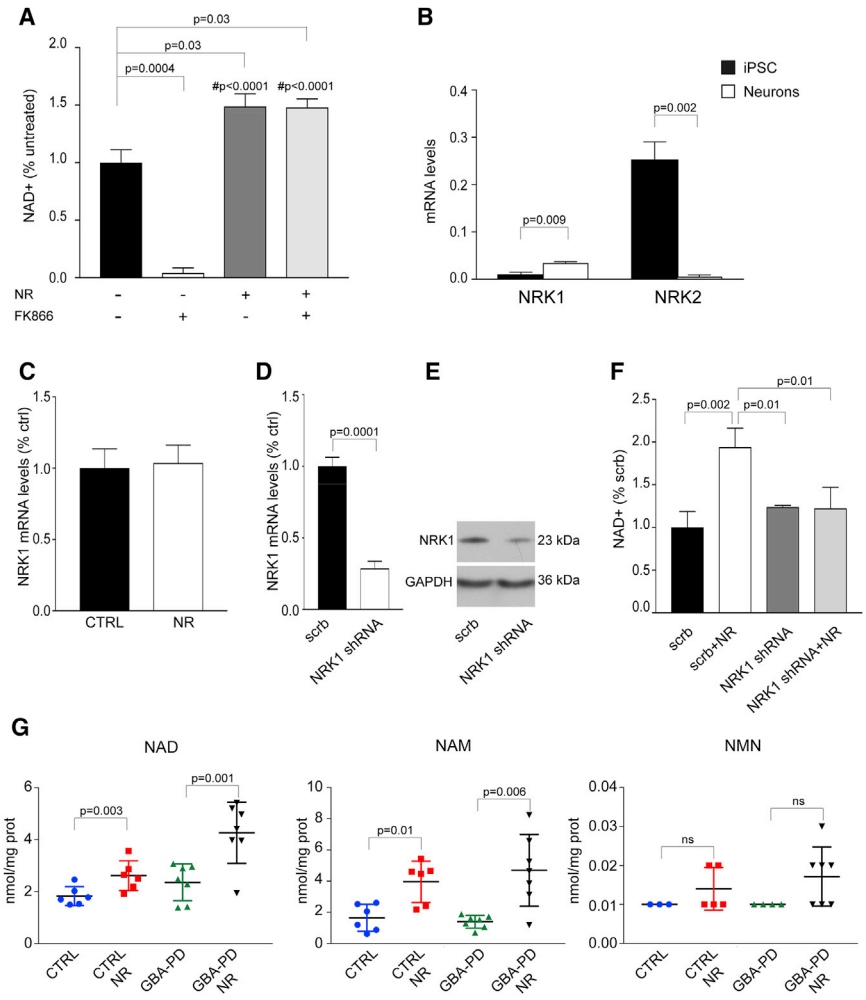

Figure 6. NR Metabolism and Availability in Human iPSC Neurons

(A) Control iPSC neurons were treated with NR with or without the NAMPT inhibitor FK866, and NAD+ levels were measured using a NAD+ cycling assay. Data are expressed as fold changes over untreated neurons and presented as mean + SEM (n = 3; one-way ANOVA). #, significance compared with FK866-treated neurons.

(B) NRK1 and NRK2 mRNA levels were measured in control undifferentiated human iPSCs and iPSC-derived neurons. Data are normalized to Rplp0 levels and expressed as mean + SEM (n = 3; two-tailed t test).

(C) NRK1 mRNA levels were measured in control iPSC neurons with or without NR treatment. Data are normalized to control and presented as mean + SEM (n = 3).

(D) Knockdown efficiency of NRK1 in iPSC neurons was determined by qRT-PCR and normalized to non-targeting shRNA. Data are presented as mean + SEM (n = 3; two-tailed t test).

(E) Representative western blot for NRK1 showing knockdown efficiency in iPSC neurons.

(F) Scramble (Scrb) or NRK1 knockdown control iPSC neurons were treated with NR, and NAD+ levels were measured using a NAD+ cycling assay. Data are expressed as fold changes over untreated and presented as mean + SEM (n = 3; one-way ANOVA).

(G) Control and *GBA*-PD (N370S) iPSC neurons were treated with 0.5 mM NR for 24 hr and LC-MS-based targeted NAD+ metabolomics was performed. Levels of NAD, NAM, and NMN are shown. Data are normalized on protein concentration and presented as mean ± SD (n = 7 independent differentiations; two-tailed t test).

lentiviral-mediated short hairpin RNA (shRNA) (Figures 6D and 6E). NRK1 knockdown did not affect basal levels of NAD+ in neurons, as assessed by a NAD+ cycling assay, whereas NR treatment was unable to significantly increase NAD+ levels in NRK1 knockdown neurons (Figure 6F). These data suggest that NRK1 is essential for exogenous NR metabolism in human neurons. To further examine the metabolism of exogenous NR, we treated control and *GBA*-PD iPSC neurons with 0.5 mM NR and performed LC-MS-based targeted quantitative metabolomics (Figures 6G and S7J). NR treatment significantly increased the levels of NAD+ in control and patient cells. In addition, we found a significant increase of NAM in both groups. On the other

(C) iPSC-derived neurons with *GBA* mutations (N370S and L444P) were treated with NR, and mRNA expression levels of mtUPR and mitochondrial biogenesis markers were measured by qRT-PCR. Data are normalized to untreated and expressed as mean + SEM (n = 5; two-tailed t test).

(D) qRT-PCR was performed to determine mtDNA content as mitochondrial (16S rRNA and tRNA-Leu) to nuclear (β-2M) DNA ratio in untreated samples or after 24- or 48-hr treatment with NR. Data are normalized to untreated and expressed as mean + SEM (n = 5; two-tailed t test).

(E) Western blot showing TOM70 levels. Protein levels are normalized to GAPDH and the corresponding untreated control. Data are presented as mean + SEM (n = 3; two-tailed t test).

(F and G) Mitochondrial morphology was assessed by TEM. Representative TEM images of mitochondria in *GBA*-PD (L444P) iPSC-derived neurons untreated or treated with NR (F; scale bar 500 nm). Quantification of mitochondrial cristae morphology in NR treated and untreated *GBA*-PD iPSC neurons (G; n = 3; two-sided Fisher's exact test).

(H) mtROS in *GBA*-PD (N370S, L444P) iPSC neurons after NR treatment. Data are normalized to the corresponding untreated control and presented as mean + SEM (n = 3; Student's t test).

(I) Mitochondrial membrane potential in *GBA*-PD (N370S, L444P) iPSC neurons after NR treatment. Data are normalized to untreated samples and presented as mean + SEM (n = 5; two-tailed t test).

(J and K) *GBA*-PD (N370S, L444P) iPSC-neurons were treated with NR, and the levels of OPA1, Mfn1, Fis1, and DRP1 were assessed by western blot (J). β-Actin was used as a loading control. Quantification is depicted in (K). Data are represented as mean + SEM (n = 5).

(L) BNIP3L mRNA levels. Data are normalized on Rplp0 and OAZ1 and expressed as fold changes over untreated. Values are presented as mean + SEM (n = 5; Student's t test).

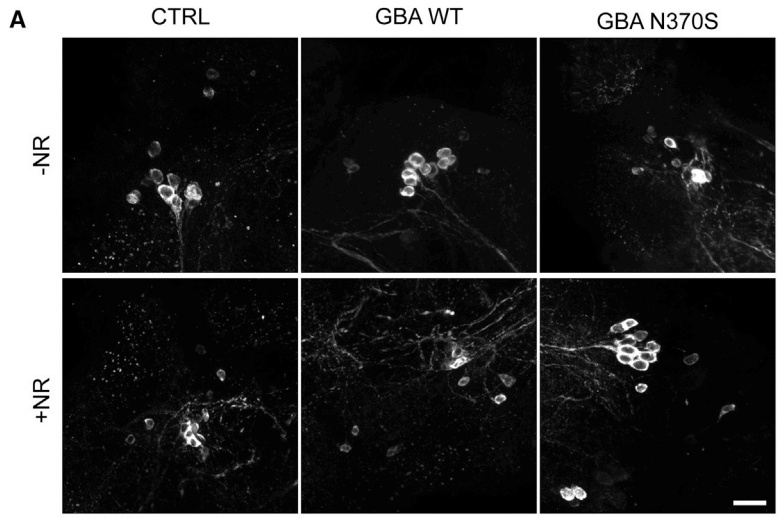

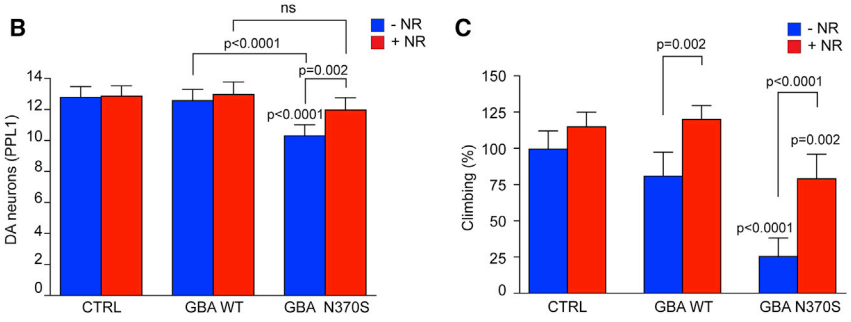

Figure 7. Nicotinamide Riboside Prevents Dopaminergic Neuronal Loss and Rescues Climbing Deficits in *GBA*-PD Flies

(A) Representative confocal images of adult *Drosophila* brains stained with anti-TH antibody. Control and transgenic flies expressing human wild-type (WT) or N370S *GBA* with and without NR treatment (500 μM for 30 days) are shown (scale bar, 10 μm).

(B) Graphs show DA cell counts in absence or presence of NR in PPL1 clusters. Data are presented as mean + SEM (ns, non-significant, n = 8–12 clusters; Kruskal-Wallis with Dunn's multiple comparisons test).

(C) Analysis of climbing ability in adult flies expressing N370S *GBA* variants in the presence or absence of NR (500 μM for 10 days). Data are presented as mean + 95% confidence interval (n = ~50 animals per condition ;Kruskal-Wallis with Dunn's multiple comparisons test).

hand, levels of NMN, the immediate downstream product of NR, tended to be higher in NR-treated cells, but this difference was not statistically significant (Figure 6G).

NR Rescues Motor Deficits in a *Drosophila* Model of *GBA*-PD

To assess the neuroprotective effect of NAD+ precursors *in vivo*, we employed a *Drosophila* model of *GBA*-PD. Flies expressing human N370S *GBA* show increased ER stress, an age-dependent loss of DA neurons accompanied by progressive defects in climbing activity (Sanchez-Martinez et al., 2016). To explore neuroprotection, flies expressing wild-type (WT) or N370S *GBA* were first raised on normal food, and then adult flies were aged on food containing NR (500 μM). At 30 days, expression of N370S *GBA* caused loss of DA neurons in the protocerebral posterial lateral 1 (PPL1) cluster. Strikingly, feeding NR significantly prevented DA neuronal loss compared to untreated controls (Figures 7A and 7B). Importantly, NR treatment also significantly prevented the decline in climbing ability in mutant N370S *GBA* flies (Figure 7C).

DISCUSSION

Mounting evidence suggests that mitochondrial dysfunction plays a key role in PD. Here, we report that neurons from *GBA*-PD patients and *GBA* KO neurons exhibit mitochondrial dysfunction characterized by morphological changes, reduced respiration, and increased oxidative stress. As mitochondrial membrane lipid composition regulates many of these functions (Aufschnaiter et al., 2017) and changes in lipid metabolism have been observed in *GBA*-PD (Schöndorf et al., 2014; Fernandes et al., 2016; García-Sanz et al., 2017), we examined the mitochondrial sphingolipid profile of *GBA*-PD and *GBA* KO neurons. Lipidomic analysis revealed the absence of a significant accumulation of sphingolipids in patient mitochondria. However, we observed a significant increase of C16-GlcCer. On the contrary, the mitochondrial sphingolipid profile of *GBA* KO neurons was profoundly altered, with significant accumulation of GlcCer and glucosylsphingosine. Given the role of sphingolipids in the regulation of mitochondrial properties, substrate accumulation or even subtle changes in lipid composition of mitochondrial membranes, as observed in patient mitochondria, may interfere with their biophysical properties and signaling pathways. However, we are not able to unambiguously define the exact subcellular localization of these alterations. Even though we have isolated mitochondria to the highest degree of purity, a small amount of contamination with lysosomes and ER was still present. The low degree of non-mitochondrial proteins and the complete absence of additional lysosomal markers (other than LAMP1) suggest the residual presence of organelle contact sites in mitochondrial preparations. Given the importance of contact sites in interorganelle communication (Wong et al., 2018), further studies are needed to investigate the role of distinct sphingolipids in such inter-organelle communication and mitochondrial dysfunction.

Overall, we did not observe a gene dosage effect when comparing mitochondrial function in heterozygous *GBA*-PD with *GBA* KO neurons. Thus, distinctly different mechanisms

likely contribute to mitochondrial dysfunction in these models. One such mechanism could be the alteration of mitochondria sphingolipid composition, which we observed in *GBA* KO, but not *GBA*-PD, cells. Interestingly, in other lysosomal storage diseases, the loss of lysosomal enzymatic function leads to substrate accumulation at the ER membranes and subsequent activation of the UPR (Tessitore et al., 2004). However, despite significant substrate accumulation in our model, the complete loss of GCase enzymatic function in *GBA* KO neurons is not sufficient to trigger ER stress responses that were instead observed in heterozygous *GBA*-PD neurons. This points toward a key role of gain-of-function mechanisms in ER stress responses in *GBA*-PD. On the other hand, GCase deficiency results in sphingolipid accumulation and mitochondrial dysfunction including increased mtROS.

GBA-PD neurons showed an imbalance of mitochondrial shaping proteins DRP1, OPA1, Mfn1, and Fis1 and an increased ratio of L-OPA1/S-OPA1. As L-OPA1 processing and impaired DRP1 activity contribute to the dysfunction of mitophagy (MacVicar and Lane, 2014), our results would suggest an impairment of mitochondrial clearance in *GBA*-PD. This was further supported by the reduced mitochondria-lysosome colocalization and reduced expression of the mitophagy adaptor NIX/BNIP3L. Unexpectedly, we did not observe a significant increase of mitochondrial content in patient neurons. The mitochondrial membrane potential was also preserved in *GBA*-PD neurons. As BNIP3L/NIX plays a role in the loss of mitochondrial membrane potential (Sandoval et al., 2008), reduced levels of BNIP3L in *GBA*-PD neurons could explain the lack of decreased mitochondrial membrane potential. Taken together, our data suggest an imbalance of mitochondrial dynamics in *GBA*-PD neurons that leads to mitochondrial dysfunction in the absence of accumulation of damaged mitochondria. As mitophagy occurs locally in distal neuronal axons, we cannot exclude accumulation of dysfunctional mitochondria within axons (Ashrafi et al., 2014).

Increasing intracellular NAD+ concentrations has been shown to be protective against age-related metabolic decline and disease (Rajman et al., 2018; Katsyuba and Auwerx, 2017). NAD+ is a coenzyme for several enzymes, including SIRT1, which regulates mitochondrial biogenesis, autophagy, and cellular stress responses (Chang and Guarente, 2014; Prola et al., 2017). Several mechanisms lead to NAD+ consumption, including oxidative stress. To examine whether NAD+ decline is involved in *GBA*-PD, we have first used targeted metabolomics and found that NAD+ levels were maintained in both *GBA*-PD and *GBA* KO iPSC-derived neurons, as well as whole brains from *gba*$^{-/-}$ zebrafish. As cellular energy metabolism and the cytosolic NADH/NAD+ redox state differ in various tissues or different cells within the same tissue, we have employed a genetically encoded NADH/NAD+ biosensor for live-cell imaging in iPSC-derived neurons. *GBA*-PD neurons showed a significant reduction of the NAD+/NADH redox state. The reduction of NMNAT2 in *GBA*-PD neurons further supports an alteration of NAD+ metabolism in *GBA*-PD. Besides its role in NAD+ synthesis, NMNAT2 also acts as a chaperone to reduce proteotoxic stress and its levels decline prior to the onset of neurodegeneration (Ali et al., 2016). Thus, the reduction of NMNAT2 in *GBA*-PD neurons could also explain the increased proteotoxic stress observed in these cells. The zebrafish metabolomics data further support an alteration of NAD+ metabolism. *GBA* deficiency led to a significant increase in NMN in zebrafish brains. This strongly suggests reduced NMNAT activity in the zebrafish brain when lacking *GBA*. We were unable to reliably detect NMN at basal conditions in iPSC-derived neurons, as NMN is a low abundance metabolite in cellular extracts. In conclusion, even though we cannot yet conclude definitively that NAD+ decline occurs in *GBA*-PD, our data suggest alterations of NAD+ metabolism in these models. Given the existence of different cellular NAD+ pools and the relevance of mitochondrial NAD+ for mitochondrial and cellular function, an important question remains how these NAD+ cellular pools communicate with each other and modulate the aging process and disease risk.

Here, we report that human iPSC-derived neurons rely on NAMPT for maintenance of the NAD+ pool, they are responsive to NAD+ precursors and utilize NRK1 as the main metabolic pathway to synthetize NAD+ from exogenous NR in a NAMPT-independent manner. NR administration caused a significant increase of NAD+. Besides NAD+, levels of NAM were also increased upon NR treatment, suggesting an increase of the activity of NAD+ consuming enzymes that convert NAD+ to NAM. However, we cannot exclude a partial conversion of exogenous NR into NAM before synthesis to NAD+. Levels of the immediate downstream product of NR, NMN, tended to be higher in NR-treated cells, but this difference was not statistically significant. This would suggest a rapid conversion of NMN into NAD+. In our model systems, NR ameliorated mitochondrial function and rescued mitochondrial quality control. We also observed an increased expression of BNIP3L/NIX after NR treatment. In line with this, mitochondrial content decreased after 24 hr of NR treatment, which points toward increased mitophagy. However, prolonged NR treatment boosted mitochondrial content and increased TFAM, which underlines the dual role of NAD+ and sirtuins in maintaining mitochondrial biogenesis and quality control. Furthermore, supporting an increase in mitophagy, NR positively regulated autophagic function. Importantly, we found that NAD+ supplementation rescues the age-dependent loss of DA neurons and decline in motor ability in a *GBA*-PD *Drosophila* model.

In summary, our study elucidates the mechanisms involved in *GBA*-PD and reveals mitochondrial dysfunction as a key driver of disease. Our findings show that NAD+ precursors ameliorate *GBA*-related defects. Among the available NAD+ precursors, NR may be a valuable therapeutic approach due to its high bioavailability, minimal toxicity, and evidence of its ability to cross the blood-brain barrier (Trammell et al., 2016). Future studies will explore the potential therapeutic benefits of combining NAD+ boosters with chaperones and GCase activators (Migdalska-Richards et al., 2016).

EXPERIMENTAL PROCEDURES

Cell Culture

iPSC lines (Table S1) were previously generated and characterized (Schöndorf et al., 2014).

Generation of *GBA* Knockout Human iPSCs

CRISPR-Cas9 constructs were generated as described previously (Ran et al., 2013).

Measurement of Mitochondrial Membrane Potential and mtROS

Neurons were washed once with Hank's balanced salt solution (HBSS) (Invitrogen) following incubation with 200 nM tetramethylrhodamine methylester perchlorat (TMRM) (Invitrogen). For measurements of mtROS, cells were incubated with 5 μM MitoSOX Red (Invitrogen). Cytofluorimetric analysis was performed using MACSQuant Analyzer 10 (Miltenyi).

Seahorse XF^{e}96 Metabolic Flux Analysis

OCR was analyzed using an XF^{e}96 Extracellular Flux Analyzer (Seahorse Biosciences).

NAD/NADH Measurements and Metabolomics

NAD+ levels were measured using the NAD/NADH-Glo Assay Kit (Promega). NADH levels were measured using the NAD/NADH Assay Kit (Abcam). The cytosolic NADH/NAD+ redox state of iPSC neurons was measured as described previously (Hung et al., 2011).

Enzymatic Activities

GCase activity was tested using the intact cell lysosomal β-Glu assay (Sawkar et al., 2006). Citrate synthase and mitochondrial CI activities were measured following the protocol reported by Spinazzi et al. (2012).

Drosophila Studies

Transgenic *Drosophila* lines expressing human WT or N370S *GBA* were previously generated (Sanchez-Martinez et al., 2016).

Statistical Analysis

The Statistical Package GraphPad Prism version 7.0b (GraphPad Software, San Diego, CA) was used to analyze the data. Statistical testing involved a two-sided Fisher's exact test, two-tailed Student's t test, one-way ANOVA with Bonferroni's multiple comparison test, or Kruskal-Wallis with Dunn's multiple comparisons test, as appropriate. Data are expressed as mean + SEM or SD as indicated.

SUPPLEMENTAL INFORMATION

Supplemental Information includes Supplemental Experimental Procedures, seven figures, and two tables and can be found with this article online at https://doi.org/10.1016/j.celrep.2018.05.009.

ACKNOWLEDGMENTS

We are grateful to Katharina Demandt, Ulrike Ulmer, Selina Reich, and Maria Zarani for their excellent experimental help and Simone Pöschel from the Imaging Flow Cytometry Core Facility, University of Tübingen for excellent assistance with the Amnis ImageStream. This work was made possible through funding by the German Research Council (DFG; DE 2157/2-1; M.D.), Helmholtz Association (VH-NG-1123; M.D.), Marie Curie Career Integration Grant (CIG304108; M.D.), Medical Research Council core funding (MC-A070-5PSB0; A.J.W.), and the European Research Council (starting grant 309742; AJW). Research was supported in part by the Medical University of South Carolina's Lipidomics Shared Resource through funding of laboratory space for the Analytical Unit located in 505 Children's Research Institute (CRI): Hollings Cancer Center (P30 CA138313), the Lipidomics Shared Resource in the South Carolina Lipidomics and Pathobiology COBRE; MUSC Department of Biochemistry (P20 RR017677), and the National Center for Research Resources and Office of the Director of the National Institutes of Health (C06 RR018823)

AUTHOR CONTRIBUTIONS

M.D. conceived, designed, and supervised the study. A.J.W. designed *Drosophila* studies. D.C.S., D.I., P.B., S.D.C., C.Y., L.K.S., G.D.N., V.P., and J.P. performed *in vitro* experiments. D.C.S., D.I., P.B., S.D.C., and L.K.S. analyzed data. S.N. and B.H. performed TEM, A.S.-M. and I.G. performed *Drosophila* studies and analyzed data, and M.K. and O.B. performed zebrafish experiments. T.G. oversaw patient sample collection. M.D. wrote the manuscript with input from all authors. All authors contributed to proofreading of the manuscript.

DECLARATION OF INTERESTS

The authors declare no competing interests.

Received: September 7, 2017
Revised: March 5, 2018
Accepted: May 2, 2018
Published: June 5, 2018

REFERENCES

Ali, Y.O., Allen, H.M., Yu, L., Li-Kroeger, D., Bakhshizadehmahmoudi, D., Hatcher, A., McCabe, C., Xu, J., Bjorklund, N., Taglialatela, G., et al. (2016). NMNAT2:HSP90 complex mediates proteostasis in proteinopathies. PLoS Biol. *14*, e1002472.

Ashrafi, G., Schlehe, J.S., LaVoie, M.J., and Schwarz, T.L. (2014). Mitophagy of damaged mitochondria occurs locally in distal neuronal axons and requires PINK1 and Parkin. J. Cell Biol. *206*, 655–670.

Aufschnaiter, A., Kohler, V., Diessl, J., Peselj, C., Carmona-Gutierrez, D., Keller, W., and Büttner, S. (2017). Mitochondrial lipids in neurodegeneration. Cell Tissue Res. *367*, 125–140.

Bieganowski, P., and Brenner, C. (2004). Discoveries of nicotinamide riboside as a nutrient and conserved NRK genes establish a Preiss-Handler independent route to NAD+ in fungi and humans. Cell *117*, 495–502.

Chang, H.C., and Guarente, L. (2014). SIRT1 and other sirtuins in metabolism. Trends Endocrinol. Metab. *25*, 138–145.

Cleeter, M.W., Chau, K.Y., Gluck, C., Mehta, A., Hughes, D.A., Duchen, M., Wood, N.W., Hardy, J., Mark Cooper, J., and Schapira, A.H. (2013). Glucocerebrosidase inhibition causes mitochondrial dysfunction and free radical damage. Neurochem. Int. *62*, 1–7.

Exner, N., Lutz, A.K., Haass, C., and Winklhofer, K.F. (2012). Mitochondrial dysfunction in Parkinson's disease: molecular mechanisms and pathophysiological consequences. EMBO J. *31*, 3038–3062.

Fernandes, H.J., Hartfield, E.M., Christian, H.C., Emmanoulidou, E., Zheng, Y., Booth, H., Bogetofte, H., Lang, C., Ryan, B.J., Sardi, S.P., et al. (2016). ER stress and autophagic perturbations lead to elevated extracellular α-synuclein in GBA-N370S Parkinson's iPSC-derived dopamine neurons. Stem Cell Reports *6*, 342–356.

García-Sanz, P., Orgaz, L., Bueno-Gil, G., Espadas, I., Rodríguez-Traver, E., Kulisevsky, J., Gutierrez, A., Dávila, J.C., González-Polo, R.A., Fuentes, J.M., et al. (2017). N370S-GBA1 mutation causes lysosomal cholesterol accumulation in Parkinson's disease. Mov. Disord. *32*, 1409–1422.

Gegg, M.E., Burke, D., Heales, S.J., Cooper, J.M., Hardy, J., Wood, N.W., and Schapira, A.H. (2012). Glucocerebrosidase deficiency in substantia nigra of Parkinson disease brains. Ann. Neurol. *72*, 455–463.

Hung, Y.P., Albeck, J.G., Tantama, M., and Yellen, G. (2011). Imaging cytosolic NADH-NAD(+) redox state with a genetically encoded fluorescent biosensor. Cell Metab. *14*, 545–554.

Jansen, I.E., Ye, H., Heetveld, S., Lechler, M.C., Michels, H., Seinstra, R.I., Lubbe, S.J., Drouet, V., Lesage, S., Majounie, E., et al.; International Parkinson's Disease Genetics Consortium (IPGDC) (2017). Discovery and functional prioritization of Parkinson's disease candidate genes from large-scale whole exome sequencing. Genome Biol. *18*, 22.

Jo, E., McLaurin, J., Yip, C.M., St George-Hyslop, P., and Fraser, P.E. (2000). alpha-Synuclein membrane interactions and lipid specificity. J. Biol. Chem. *275*, 34328–34334.

Katsyuba, E., and Auwerx, J. (2017). Modulating NAD$^+$ metabolism, from bench to bedside. EMBO J. *36*, 2670–2683.

Keatinge, M., Bui, H., Menke, A., Chen, Y.C., Sokol, A.M., Bai, Q., Ellett, F., Da Costa, M., Burke, D., Gegg, M., et al. (2015). Glucocerebrosidase 1 deficient

Danio rerio mirror key pathological aspects of human Gaucher disease and provide evidence of early microglial activation preceding alpha-synuclein-independent neuronal cell death. Hum. Mol. Genet. *24*, 6640–6652.

MacVicar, T.D., and Lane, J.D. (2014). Impaired OMA1-dependent cleavage of OPA1 and reduced DRP1 fission activity combine to prevent mitophagy in cells that are dependent on oxidative phosphorylation. J. Cell Sci. *127*, 2313–2325.

Magalhaes, J., Gegg, M.E., Migdalska-Richards, A., Doherty, M.K., Whitfield, P.D., and Schapira, A.H. (2016). Autophagic lysosome reformation dysfunction in glucocerebrosidase deficient cells: relevance to Parkinson disease. Hum. Mol. Genet. *25*, 3432–3445.

Maor, G., Rencus-Lazar, S., Filocamo, M., Steller, H., Segal, D., and Horowitz, M. (2013). Unfolded protein response in Gaucher disease: from human to Drosophila. Orphanet J. Rare Dis. *8*, 140.

Mazzulli, J.R., Xu, Y.H., Sun, Y., Knight, A.L., McLean, P.J., Caldwell, G.A., Sidransky, E., Grabowski, G.A., and Krainc, D. (2011). Gaucher disease glucocerebrosidase and α-synuclein form a bidirectional pathogenic loop in synucleinopathies. Cell *146*, 37–52.

Migdalska-Richards, A., and Schapira, A.H. (2016). The relationship between glucocerebrosidase mutations and Parkinson disease. J. Neurochem. *139* (*Suppl 1*), 77–90.

Migdalska-Richards, A., Daly, L., Bezard, E., and Schapira, A.H. (2016). Ambroxol effects in glucocerebrosidase and α-synuclein transgenic mice. Ann. Neurol. *80*, 766–775.

Mouchiroud, L., Houtkooper, R.H., Moullan, N., Katsyuba, E., Ryu, D., Cantó, C., Mottis, A., Jo, Y.S., Viswanathan, M., Schoonjans, K., et al. (2013). The NAD(+)/sirtuin pathway modulates longevity through activation of mitochondrial UPR and FOXO signaling. Cell *154*, 430–441.

Osellame, L.D., Rahim, A.A., Hargreaves, I.P., Gegg, M.E., Richard-Londt, A., Brandner, S., Waddington, S.N., Schapira, A.H., and Duchen, M.R. (2013). Mitochondria and quality control defects in a mouse model of Gaucher disease: links to Parkinson's disease. Cell Metab. *17*, 941–953.

Prola, A., Pires Da Silva, J., Guilbert, A., Lecru, L., Piquereau, J., Ribeiro, M., Mateo, P., Gressette, M., Fortin, D., Boursier, C., et al. (2017). SIRT1 protects the heart from ER stress-induced cell death through eIF2α deacetylation. Cell Death Differ. *24*, 343–356.

Rajman, L., Chwalek, K., and Sinclair, D.A. (2018). Therapeutic potential of NAD-boosting molecules: the in vivo evidence. Cell Metab. *27*, 529–547.

Ran, F.A., Hsu, P.D., Wright, J., Agarwala, V., Scott, D.A., and Zhang, F. (2013). Genome engineering using the CRISPR-Cas9 system. Nat. Protoc. *8*, 2281–2308.

Rocha, E.M., Smith, G.A., Park, E., Cao, H., Brown, E., Hallett, P., and Isacson, O. (2015). Progressive decline of glucocerebrosidase in aging and Parkinson's disease. Ann. Clin. Transl. Neurol. *2*, 433–438.

Sanchez-Martinez, A., Beavan, M., Gegg, M.E., Chau, K.Y., Whitworth, A.J., and Schapira, A.H. (2016). Parkinson disease-linked GBA mutation effects reversed by molecular chaperones in human cell and fly models. Sci. Rep. *6*, 31380.

Sandoval, H., Thiagarajan, P., Dasgupta, S.K., Schumacher, A., Prchal, J.T., Chen, M., and Wang, J. (2008). Essential role for Nix in autophagic maturation of erythroid cells. Nature *454*, 232–235.

Sawkar, A.R., Schmitz, M., Zimmer, K.P., Reczek, D., Edmunds, T., Balch, W.E., and Kelly, J.W. (2006). Chemical chaperones and permissive temperatures alter localization of Gaucher disease associated glucocerebrosidase variants. ACS Chem. Biol. *1*, 235–251.

Schapira, A.H., Cooper, J.M., Dexter, D., Jenner, P., Clark, J.B., and Marsden, C.D. (1989). Mitochondrial complex I deficiency in Parkinson's disease. Lancet *1*, 1269.

Schöndorf, D.C., Aureli, M., McAllister, F.E., Hindley, C.J., Mayer, F., Schmid, B., Sardi, S.P., Valsecchi, M., Hoffmann, S., Schwarz, L.K., et al. (2014). iPSC-derived neurons from GBA1-associated Parkinson's disease patients show autophagic defects and impaired calcium homeostasis. Nat. Commun. *5*, 4028.

Sidransky, E., Nalls, M.A., Aasly, J.O., Aharon-Peretz, J., Annesi, G., Barbosa, E.R., Bar-Shira, A., Berg, D., Bras, J., Brice, A., et al. (2009). Multicenter analysis of glucocerebrosidase mutations in Parkinson's disease. N. Engl. J. Med. *361*, 1651–1661.

Spinazzi, M., Casarin, A., Pertegato, V., Salviati, L., and Angelini, C. (2012). Assessment of mitochondrial respiratory chain enzymatic activities on tissues and cultured cells. Nat. Protoc. *7*, 1235–1246.

Tessitore, A., del P Martin, M., Sano, R., Ma, Y., Mann, L., Ingrassia, A., Laywell, E.D., Steindler, D.A., Hendershot, L.M., and d'Azzo, A. (2004). GM1-ganglioside-mediated activation of the unfolded protein response causes neuronal death in a neurodegenerative gangliosidosis. Mol. Cell *15*, 753–766.

Trammell, S.A., Schmidt, M.S., Weidemann, B.J., Redpath, P., Jaksch, F., Dellinger, R.W., Li, Z., Abel, E.D., Migaud, M.E., and Brenner, C. (2016). Nicotinamide riboside is uniquely and orally bioavailable in mice and humans. Nat. Commun. *7*, 12948.

Velayati, A., Yu, W.H., and Sidransky, E. (2010). The role of glucocerebrosidase mutations in Parkinson disease and Lewy body disorders. Curr. Neurol. Neurosci. Rep. *10*, 190–198.

Wong, Y.C., Ysselstein, D., and Krainc, D. (2018). Mitochondria-lysosome contacts regulate mitochondrial fission via RAB7 GTP hydrolysis. Nature *554*, 382–386.

Cell Reports, Volume *23*

Supplemental Information

The NAD+ Precursor Nicotinamide Riboside Rescues Mitochondrial Defects and Neuronal Loss in iPSC and Fly Models of Parkinson's Disease

David C. Schöndorf, Dina Ivanyuk, Pascale Baden, Alvaro Sanchez-Martinez, Silvia De Cicco, Cong Yu, Ivana Giunta, Lukas K. Schwarz, Gabriele Di Napoli, Vasiliki Panagiotakopoulou, Sigrun Nestel, Marcus Keatinge, Jan Pruszak, Oliver Bandmann, Bernd Heimrich, Thomas Gasser, Alexander J. Whitworth, and Michela Deleidi

Supplemental Experimental Procedures

Material and reagents

Nicotinamide riboside hydrochloride was provided by ChromaDex, Inc. and dissolved in water.

Cell culture and treatments

The iPSC lines used in this study were previously generated from GBA-PD patients and control individuals and characterized (Schöndorf et al., 2014). The list of the lines is provided in Table S1. For all iPSC lines, informed consent was obtained from patients prior to cell donation using a written form. The protocol was approved by the Ethics Committee of the Medical Faculty and the University Hospital Tübingen (Ethikkommission der Medizinischen Fakultät am Universitätsklinikum Tübingen). iPSCs were maintained in hESC medium containing knockout DMEM (Gibco Life Technologies), 20% knockout serum replacement (Gibco Life Technologies), 1% non-essential amino acids (Gibco Life Technologies), 1% penicillin/streptomycin (P/S, Merck Millipore), 1% GlutaMAX Supplement (Gibco Life Technologies) and 500 µM β-mercaptoethanol (Sigma-Aldrich) supplemented with 10 ng/ml FGF2 (Peprotech). iPSCs were routinely passaged onto MMC-treated CF-1 mouse embryonic fibroblasts (MEF) (Globalstem MTI ThermoFisher) with addition of 10 µM Rock inhibitor Y-27632 2HCl (Selleckchem). iPSCs were differentiated into dopaminergic neurons according to Kriks et al. (Kriks et al., 2011). Cells were grown for 11 days on Matrigel (Corning) in hESC medium. Differentiation was based on exposure to LDN193189 (100 nM, Axon Medchem) from days 0–11, SB431542 (10 µM, Selleckchem) from days 0–5, SHH (100 ng/mL, Peprotech), purmorphamine (PMA; 2 µM, EMD) and FGF8 (100 ng/mL, Peprotech) from days 1–7 and CHIR99021 (CHIR; 3 µM, Axon Medchem) from days 3–13. hESC medium was gradually shifted to N2 medium (DMEM/Ham's F12 , 1% P/S, 1% GlutaMAX and N2 supplement from Gibco Life Technologies), starting on day 5 of differentiation. On day 11, medium was changed to N2/B27 medium containing DMEM/Ham's F12, Neurobasal medium, N2 and B27 supplement, 1% P/S and 1% Glutamax (N2 and B27 supplement; Gibco Life Technologies) supplemented with CHIR (3 µM, until day 13) and brain-derived neurotrophic factor (BDNF; 20 ng/ml; Peprotech), ascorbic acid (AA; 200 µM, Sigma-Aldrich), glial cell line-derived neurotrophic factor (GDNF; 20 ng/ml; Peprotech), transforming growth factor type β3 (TGFβ3, 1 ng/ml; Peprotech), dibutyryl cAMP (0.5 mM; Applichem), and DAPT (10 µM; Selleckchem) for 9 days. On day 20, cells were dissociated using Accutase (Sigma-Aldrich) and replated under high cell density conditions on dishes pre-coated with 15 µg/ml polyornithine and 1 µg/ml laminin in differentiation medium (N2/B27 medium +BDNF, AA, GDNF, dbcAMP, TGFβ3 and DAPT). Neurons were maintained *in vitro* for 45-55 days and then used for experiments. For metabolomics after NR treatment, iPSCs were differentiated into dopaminergic neurons using a previously published protocol (Reinhardt et al., 2013). iPSC colonies were manually detached 3–4 days after splitting and resuspended in hESC medium (without FGF2) supplemented with 10 µM SB431542 (Selleckchem), 1 µM dorsomorphin (Sigma-Aldrich), 3 µM CHIR 99021, and 0.5 µM PMA. Medium was replaced on day 2 by N2/B27 medium supplemented with the same small molecule supplements. On day 4, SB-431542 and dorsomorphin were withdrawn and 150 µM AA was added to the medium. On day 6, embryoid bodies were manually triturated and plated on Matrigel-coated 12-well plates in N2/B27 medium supplemented with CHIR, PMA, and AA. Neural precursor cells (NPCs) were regularly split with Accutase at a 1:10 ratio every 5-6 days and used for experiments at passage number 10-12. Expansion medium consisted of N2/B27 medium freshly supplemented with CHIR, PMA, and AA. For differentiation into DA neurons, expansion medium was changed 2 days after splitting to N2/B27 medium with 100 ng/mL FGF8, 1 µM PMA,

and 200 µM AA. After 8 days, maturation medium consisting of N2/B27 medium with 10 ng/mL BDNF, 10 ng/mL GDNF, 1 ng/mL TGFβ3, 200 µM AA, 500 µM dbcAMP, and 0.5 µM PMA (for 2 more days) was used. One day after changing to maturation medium, the cultures were dissociated with Accutase and split at a 1/3 ratio. Cultures were analyzed after 2 weeks in maturation medium.

The quality of iPSCs and iPSC-derived neurons was checked every two months for the presence of mycoplasma. Sanger sequencing was performed every three months to check for iPSC line identity. The quality of neuronal cultures was checked by confirmation of the presence of neuronal and dopaminergic markers by immunostaining for β-III Tubulin and TH. Only neuronal cultures that passed quality checks were used for further experiments. iPSC-derived neurons were treated with 0.5 mM NR (ChromaDex, Inc) or 1 µM PJ34 (Tocris) for 24 or 48 h (where indicated). The following reagents were used: 0.5 mM ß-nicotinamide mononucleotide (NMN; Sigma-Aldrich), 0.5 mM nicotinamide (NAM, Sigma-Aldrich), 1 nM FK866 (Sigma-Aldrich), 100 nM EX527 (Tocris). Appropriate vehicle control was used.

Generation of *GBA* knockout human iPSCs with CRISPR-Cas9

CRISPR-Cas9 constructs used in this study were generated as described by Ran et. al (Ran et al., 2013). The pSpCas9(BB)-2A-Puro plasmid containing the sgRNA scaffold and a puromycine resistance under the U6 promoter was purchased from Addgene (Addgene plasmid #48139). sgRNAs targeting exon 3 and exon 4 of the *GBA* locus with low predicted off target effects were designed using the CRISPR Design Tool (http://tools.genome-engineering.org) and purchased at Metabion International AG. sgRNA sequences: GBA Exon 3 top TACACGCAGTGGGCGACGGA; GBA Exon 3 bottom TCCGTCGCCCACTGCGTGTA; GBA Exon 4 top GGAACTTCTGTTCTGGCTGC; GBA Exon 4 bottom GCAGCCAGAACAGAAGTTCC. Successful integration of the sgRNAs in the pSpCas9 plasmid was confirmed by Sanger sequencing using a primer pairing in the U6 promoter region. iPSCs were dissociated using 0.02% EDTA and $1x10^5$ cells were nucleofected with 7 µg sgRNA containing pSpCasp9 plasmids targeting exon 3 and exon 4 of the *GBA* gene using an Amaxa Nucleofector II (program B16). After nucleofection, iPSCs were replated onto MEF-coated dishes in hESC medium containing 10 µM ROCK inhibitor without P/S. The next day the medium was replaced with mTeSR (StemCell Technologies) containing 0.5 µg/ml puromycin (Sigma-Aldrich) for 48 h. After 5-7 days, single colonies were manually picked and transferred on MEF-coated plates for further expansion. To check for Cas9-induced double-strand breaks, DNA was isolated and the exon 1-5 region of the *GBA* gene was amplified. The resulting PCR product was purified and the exon 3-4 region was amplified to check for genomic deletions on a 1.5% agarose gel. Genomic deletions in *GBA* knockout iPSCs were confirmed by Sanger sequencing. The following primers were used:

Primer for *GBA* exon 3 and 4 amplification and sequencing (5'-3')		
GBA Exon 1-5	FW	CCTAAAGTTGTCACCCATAC
	RV	AGCAGACCTACCCTACAGTTT
GBA Exon 3	FW	ATGTGTCCATTCTCCATGTC
	RV	GGTGATCACTGACACCATTT
GBA Exon 4	FW	GGTGTCAGTGATCACCATGG
	RV	ACGAAAAGTTTCAATGGCTCT

The off-target loci with the highest prediction scores for each sgRNA were sequenced by Sanger sequencing.

Sequencing primers for off-target effect (5'-3')		
CAMTA2	FW	TTCCGTCCTCCTCCCCC
	RV	GAGTGGTGGTCCCAGGAGAA
UBA7	FW	TCCCTGAACCTCAGCCTGTC
	RV	AGCCTCAAGGGGTGGGGTTA
P2RX2	FW	CGTGTTCAGCATCATCACCAGG
	RV	AGAGGTCACTGAGGCATTAGC
TMEM31	FW	ATGGCAGCATACTCCAGCAA
	RV	TGAACGCTGCCTGACCAATTA
GGCX	FW	CAGGCAGGGATCTCGTTGTG
	RV	CAATACCAGGAAGCAAGGGCT
SYT7	FW	TCTCCCTTCCTTCTCAGGGG
	RV	AAATCTGCCGTCTCCAAGGG
PLEKHH2	FW	ACTCAGAGCTGGTGTTTGGC
	RV	GAGGCTCAATCTGACTGACTGC
PLEKHM2	FW	ACTGCCTAGGACCACTGACG
	RV	GGGAGGCAAGCATAGTGTCT
LOC100505795	FW	ACAACAGACAGAGCGGCAAG
	RV	ATCTTTCTTGCCTCGAGGGTG
SPTB	FW	CAGAAGGGGCAGTCCCAAGA
	RV	GCCCCACCTGCTACTTCTTTT
FGFR1OP	FW	CACCAGTGTTGCTGCTTTGTG
	RV	TGACAGCGCCTGATCACTTC
ZKSCAN1	FW	GGCTGCGGCCAGAAATAAAC
	RV	GTTTCAACGTCTGTGCCCTG

Measurement of mitochondrial membrane potential

For measurement of mitochondrial membrane potential, neurons were split at a concentration of $2x10^5$/well on 96-wells pre-coated with Matrigel. Cells were kept in N2 medium for 24 h. Cells were washed once with HBSS (Invitrogen) following incubation with 200 nM Tetramethylrhodamine Methylester Perchlorat (TMRM) (Invitrogen) in HBSS with 1% BSA for 30 min at 37°C. Cells were then washed twice with HBSS, detached using Accumax (Invitrogen) and kept in HBSS with 1% BSA (Sigma-Aldrich) for FACS analysis using MaxQuant Analyzer 10 (Miltenyi Biotec). Analysis was performed using the MACSQuantify 2.6 software (Miltenyi Biotec).

Measurement of mitochondrial ROS

For measurement of mtROS, neurons were split at a concentration of $2x10^5$/well on 96-wells pre-coated with Matrigel. iPSC-derived neurons were pre-incubated with N2 medium for 48 h. Next, cells were washed once with HBSS, incubated with 5µM MitoSOX Red (Invitrogen) for 30 min at 37°C, washed twice with HBSS, trypsinized and resuspended in 200µl of HBSS and 1% BSA. Cytofluorimetric analysis was performed using MACSQuant Analyzer 10 (Miltenyi BIotec).

Seahorse XF^{e}96 Metabolic Flux Analysis

Oxygen consumption rate was analyzed using an XF^{e}96 Extracellular Flux Analyzer (Seahorse Biosciences). iPSC-derived neurons were plated on V3-PS XF plates (Seahorse Biosciences) at a density of 5 x10^{4}/well per well and grown in N2 medium for 48 h before the experiment. Respiration was measured after sequential injection of 1µM oligomycin, 5µM carbonyl cyanide p-trifluoromethoxyphenylhydrazone (CCCP) and 1µM rotenone and 1µM Antimycin A (all from Sigma-Aldrich). After each injection, OCR was measured for 2 minutes, the medium was mixed for 2 min, and then respiration was measured again for 2 minutes. Values were normalized to cell number by counting DAPI stained nuclei using a high-content cell analyzer (BD Bioscience, Pathway 855).

Western blot

Proteins were extracted using Tris-buffered Saline (TBS) with 0.5% NP40 lysis buffer containing protease and phosphatase inhibitors (Roche) on ice following centrifugation at 14.000 rpm and 4°C for 15min. The protein concentration of the supernatant was determined by BCA (Pierce). In total, 15–30 µg of the protein lysate was loaded on a 7% to 15% polyacrylamide gel and transferred on a PVDF membrane (Millipore). Isoforms of OPA1 were resolved on a 7% polyacrylamide gel and corresponding higher (~100kDa) and lower (~80kDa) bands were used for densitometric analysis to obtain the L-OPA1/S-OPA1 ratio. Blots were blocked with 5% milk or 5% BSA in TBS + 0.1% Tween 20 (TBST) and incubated with primary antibodies in blocking solution (Western Blotting Reagent, Roche) overnight at 4 °C. This step was followed by incubation with corresponding HRP-conjugated secondary antibodies (Sigma-Aldrich) for 1 h at room temperature. Visualization of proteins was done by using Amersham ECL Western Blotting Detection Reagent and Amersham Hyperfilm (both GE healthcare). Densitometric analysis of proteins was performed by ImageJ software.

Immunofluorescence

Cells were fixed in 4% paraformaldehyde (PFA) in PBS (w/v) for 10 min, rinsed with PBS and blocked by 10% normal goat or donkey serum (NGS/NDS) in PBST (PBS + 0.1% TritonX-100) for 60 min. Cells were then incubated with primary antibodies in 10% NGS/NDS in PBST over night at 4°C following 1h incubation at 24°C with appropriate Alexa488/568/647 coupled secondary antibodies (Invitrogen). Cell nuclei were stained with Hoechst and final images were acquired with a Zeiss Imager Z1 with Apotome (Carl Zeiss) microscope using a 63x 1.4NA plan-apochromat oil objective. For mitochondrial lysosomal co-localization analysis, Z-stack pictures of single cells were obtained with a Leica TCS SP8 X confocal microscope (Leica Biosystems) using a 63x 1.4NA plan-apochromat oil objective. Images were processed in ImageJ (NIH) and brightness/contrast was adjusted equally.

Zebrafish experiments

Zebrafish were raised at a density of 20 individuals per tank until 12 weeks of age. Animals were then culled, brains extracted and flash frozen. Samples were stored at -80 °C until use. Each animal was genotyped using primers FW 5' AAAGCAGCACGATATGTCCA and RV 5' ATGTCATGGGCGTAGTCCTC as previously described (Keatinge et al., 2015).

ImageStream

Cells were fixed in 1% PFA, permeabilized and blocked in 10% FBS/0.1%Triton X solution. Intracellular staining was performed with anti-rabbit TOMM20 and anti-mouse LAMP1 antibodies. Staining was detected with Alexa Fluor 488/568 secondary antibodies (Invitrogen). Images were acquired on an Amnis ImageStream 100 imaging flow cytometer (EMD Millipore) with a 40x or 60x magnification with a minimum of 10,000 events acquired per sample. Single stained samples were used to create a compensation matrix. Double positive cells were gated, and Bright Detail Similarity Feature was applied to calculate co-localization score between TOMM20 and LAMP1 signals with Amnis IDEAS software (EMD Millipore). Cells treated with 10μM CCCP for 24 hours were used as positive control.

NAD/NADH measurements and metabolomics

To measure NAD+ levels, $4x10^5$ iPSC-derived neurons were harvested and analysed using the NAD/NADH-Glo™ Assay Kit (Promega) following the manufacturer´s instructions. To measure NADH levels, $1×10^6$ iPSC-derived neurons were harvested and the NAD/NADH Assay Kit (Abcam) was used following the manufacturer's instructions. For cell metabolomics, cells were differentiated onto 6-well plates, washed once with ice-cold PBS and snap frozen on dry ice. The plates were kept at -80°C until shipment. Metabolomics analysis was performed at the Southeast Center for Integrated Metabolomics (SECIM) at Sanford-Burnham-Prebys Medical Discovery Institute, following protocols as defined on the Metabolomics Workbench. For zebrafish metabolomics, frozen zebrafish brains from *gba*$^{+/+}$, *gba*$^{+/-}$ and *gba*$^{-/-}$ (each n=6) were received on dry ice and lyophilized to dryness overnight. Groups of three freeze-dried brains were pooled for each sample. For oxidized nucleotides, cell slush on ice was vortexed with 200 μL of 1 M perchloric acid and brought up to a volume of 400 μL with deionized water. A 100 μL aliquot of homogenate was used to measure reduced pyridine nucleotides. The homogenate was centrifuged at 14,000 rpm at 10 °C for 5 minutes. Then, the supernatant was neutralized with 100 μL of 1 M ammonium formate. Oxidized nucleotides were analyzed using a Dionex 3000 HPLC/Thermo Scientific triple quadrupole mass spectrometer, and quantified according to calibration curves obtained from neat standards using 18O2-NMN and 18O2-NAD as internal standards. For reduced nucleotides, cell slush on ice was vortexed with 200 μL of NaOH and 8 mL of 5 M NaOH, and brought to a volume of 400 μL with deionized water. 200 μL aliquot of homogenate was used to measure reduced pyridine nucleotides. The homogenate was centrifuged at 14,000 rpm at 10 °C for 5 minutes. Then, the supernatant was analyzed using a Dionex 3000 HPLC/Thermo Scientific triple quadrupole mass spectrometer. NADH and NADPH in unknown samples were quantitated according to calibration curves obtained from neat standards using 18O2-NADH as an internal standard.

Cytosolic NADH/NAD+ redox state

The cytosolic NADH/NAD+ redox state of iPSC-derived neurons was measured following a protocol previously described by Hung et al (Hung et al., 2011, Hung and Yellen, 2014). iPSC-derived neurons were transfected with GW1-Peredox-mCherry (Addgene #32380) using Viafect transfection reagent (Promega). Cells were chosen based on neuronal morphology and imaged live in a humidified chamber with 5% CO_2 and 37°C using a Zeiss Axio Observer Z1 (Carl Zeiss) microscope with a 63x 1.4NA plan-apochromat oil objective. For final NADH/NAD quantification, Peredox signal was normalized to mCherry signal using Image J. NR-treated cells were used as positive control.

Quantitative RT-PCR

mRNA was isolated using a RNA isolation kit (Qiagen). Following the reverse transcription reaction using the QuantiTect Reverse Transcription kit, quantitative PCR reaction was performed using QuantiTect SYBR GREEN I kit (Qiagen) and monitored with a Viia7 Real time PCR system (Applied Biosystems). The expression level of each gene was normalized to the housekeeping genes ribosomal protein large P0 (Rplp0) and ornithine decarboxylase antizyme 1 (OAZ) as indicated. Fold-changes in gene expression were calculated using the 2^{-DDCT} method, based on biological reference samples and housekeeping genes for normalization.

Primers used for quantitative PCR (5'-3')		
OAZ	FW	AGCAAGGACAGCTTTGCAGTT
	RV	ATGAAGACATGGTCGGCTCG
RPLP0	FW	CCTCATATCCGGGGGAATGTG
	RV	GCAGCAGCTGGCACCTTATTG
HSP60	FW	TGACCCAACAAAGGTTGTGA
	RV	CATACCACCTCCCATTCCAC
TFAM	FW	GCTTGGAAAACCAAAAAGACCTCGT
	RV	GTCTTCAGCTTTTCCTGCGGTG
PGC1a	FW	TGAAAAAGCTTGACTGGCGT
	RV	GTCACTGCACCACTTGAGTC
GBA	FW	ACCCTAGGGGAGACACACCG
	RV	AATTGGGTCCTCCTTCGGGG
Sirt1	FW	GAGCTGGGGTGTCTGTTTCA
	RV	TTTGGATTCCCGCAACCTGT
XBP1S	FW	TGCTGAGTCCGCAGCAGGTG
	RV	GCTGGCAGGCTCTGGGGAAG
BNIP3L	FW	CAGCAGGGACCATAGCTCTC
	RV	TCCTTGGGTGGAATGTTTTC
NAMPT	FW	ATCCTGTTCCAGGCTATTCTGT
	RV	CCCCATATTTTCTCACACGCAT
NMNAT2	FW	GATCCTGCTGCTGTGTGGTA
	RV	ACCACCACAATCCCAAAGTC
NMNAT1	FW	AAAGAAATCCCTAGAGCCAAAA
	RV	TCCAGCCCGAGTAACACATA
NMNAT3	FW	CACGACCCAAAAGGTTACATC
	RV	TGACAGCATCGGGAATCA
NMRK1	FW	GGATGGAAAGCGCAAGACAC
	RV	ATGGCCATCAAAGTATCCCG
NMRK2	FW	ACCGTCCCGTATGAAGAGTG
	RV	AGAGCTCCTCTCGGGACTTC

Mitochondrial DNA content

Genomic and mitochondrial DNA (mtDNA) was isolated using the Blood and Tissue DNA isolation Kit (Qiagen) following the manufacturer's instructions. Real-time quantification of DNA targets was performed using the

QuantiTect SYBR Green Kit (Qiagen) and respective primers (see list below for primers used) on a ViiA7 Real-Time PCR System (Applied Biosystems). Fold changes of mtDNA abundance were calculated using the 2^{-DDCT} method and normalized to the biological reference sample and the genomic housekeeping gene beta-2-microglobulin (b-2M).

Primers for mitochondrial content quantification (5'-3')		
tRNALeu	FW	CACCCAAGAACAGGGTTTGT
	RV	TGGCCATGGGTATGTTGTTA
β2-microglobulin	FW	TGCTGTCTCCATGTTTGATGTATCT
	RV	TCTCTGCTCCCCACCTCTAAGT
16S rRNA	FW	GCCTTCCCCCGTAAATGATA
	RV	TTATGCGATTACCGGGCTCT

Enzymatic activities

GCase enzymatic activity was tested using the intact cell lysosomal β-Glu assay with slight modifications (Sawkar et al., 2006). iPSC-derived neurons were plated onto Matrigel-coated 48-well plates in differentiation medium (5 $x10^4$ cells/well). For CBE-sensitive GCase assay, the cells were pre-incubated for 30 min at room temperature in McIlvaine Buffer (0.1 M Citrate/0.2 M Phosphate) pH 6.0 containing 5 nM AMP-DNM N-(5-adamantane-1-yl-methoxy-pentyl)-deoxynojirimycin). After incubation with the inhibitor, 4-methylumbelliferyl-β-D-glucopyranoside (MUB-Glc, Glycosynth) was added at a final concentration of 3 mM. The reaction mixtures were incubated at 37 °C under gentle shaking. The fluorescence was recorded after transferring 20 µl of the reaction mixtures to a microplate and adding 180 µl of 0.25 M glycine, pH 10.7. Citrate synthase and mitochondrial complex I activities were measured from mitochondrial-enriched fractions following the protocol reported by Spinazzi et al. (Spinazzi et al., 2012). Complex I data were normalized to citrate synthase activity.

Autophagy studies

Where indicated, cells were treated with NH_4Cl (20 mM) and leupeptin (200 µM) (EMD, Millipore) for 4 h. LC3-II and LC-I levels were quantified by densitometry and normalized to β-actin. LC3 flux was quantified as the change in LC3-II levels in the presence and in the absence of lysosomal inhibitors.

Mitochondrial isolation and lipidomic analysis

The mitochondrial isolation was performed with the Qproteome® Mitochondria Isolation Kit (Qiagen) according to the supplier's protocol. iPSC-derived neurons were washed with cold PBS, lysed, and centrifuged at 1,000 g for 10 minutes at 4°C. The supernatants were collected (cytosolic fraction), and the pellets were washed twice with cold PBS, resuspended and sheared via passage 20-30 times through a 26-gauge needle. The lysates were then centrifuged at 1,000 x g for 10 minutes at 4°C, and the supernatant fractions, containing the mitochondria, were centrifuged again at 6,000 x g for 10 minutes at 4°C. After determining the protein concentration, purity was confirmed by Western blot. Mitochondrial fractions were lyophilized and subjected to lipidomic analysis. Analyses of all sphingolipids (total and mitochondrial) were performed by high-performance liquid chromatography mass spectrometry (LC-MS/MS) methodology at MUSC Lipidomics Shared Resource at the Medical University of South Carolina as previously described (Bielawski et al., 2009). Lipids were extracted from frozen cell pellets or

mitochondrial extracts from iPSC-neurons. Quantitative analyses of sphingolipids are based on eight-point calibration curves generated for each target analyte. The synthetic standards along with a set of internal standards are spiked into an artificial matrix; they are then subjected to an identical extraction procedure as the biological samples. These extracted standards are then analyzed by the HPLC/MS/MS or SFC/MS/MS system operating in positive MRM mode employing a gradient elution. The equipment consisted of a Thermo Scientific Accela Autosampler and Quaternary Pump coupled to a Thermo Scientific Quantum Access triple quadrupole mass spectrometer equipped with an ESI probe operating in the multiple reaction monitoring positive ion mode. Separation of Glu-Cer was performed by SFC-MS/MS analyses employing the same mass spectrometer tuned and optimized for the Waters UPC 2 system. Chromatographic separations were obtained utilizing a carbon dioxide gas and 1 mM ammonium formate in 0.2% formic acid in methanol mobile phase. Chromatographic separations were obtained under a gradient elution for both assays. Peaks for the target analytes and internal standards are recorded and processed using the instrument's software system. Plotting the analyte/internal standard peak area ratios against analyte concentrations generates the analyte specific calibration curves. Any sphingolipid for which no standards are available are quantitated using the calibration curve of its closest counterpart. Lipid levels were expressed as pmol lipid level/ nmol Pi. The analysis was repeated from independent differentiation onsets (n for each experiment is indicated in figure legend).

Lentivirus-mediated shRNA

The Mission lentiviral plasmids encoding turbo GFP (SHC003), non-targeting control shRNA (SHC016) and NRK1 shRNA (TRCN0000160469, TRCN0000160349) in pLKO.1-puro vector backbone were used (from Sigma-Aldrich). Lentiviral stocks were prepared by calcium phosphate transfection and the packaging vectors pLP1, pLP2 and pLP/VSVG using the ViraPower HiPerform T-REx Gateway Expression System (Invitrogen). Supernatants were collected over 48 to 60 h and virus with minimal MOI 5x 105 IFU/ml was concentrated and used to infect cells.

Transmission electron microscopy and analysis of mitochondrial morphology

After washing with 0.1 M PB cells were processed in 1% osmium tetroxide / 6.85% sucrose in 0.1 M PB for 1 h. Samples were dehydrated using increasing ethanol concentrations (20%-100%) for each 10 minutes, with incubation steps using 1% uranyl acetate in 70% ethanol for 1h in between. Samples were then incubated twice for 5 min with propylene oxide before embedding in Durcupan (Sigma-Aldrich) overnight. Ultrathin sections (60 nm) were cut and stained with lead citrate (Reynolds). Images were taken with a TEM LEO 906 microscope (Zeiss) with the sharp-eye 2k CCD camera and processed with ImageSP (Tröndle, Germany). Morphometric classification of mitochondrial cristae morphology on EM pictures was performed blindly on at least 50 cells per condition from independent experiments. Individual cells were scored for normal (lamellar) or ballooned/swollen cristae (disorganized). Mitochondrial major diameter was measured blindly using NIH Image J software.

***Drosophila* studies**

Transgenic *Drosophila* lines expressing human wt or N370S *GBA* were previously generated (Sanchez-Martinez et al., 2016). Flies were raised under standard conditions at 25 °C on agar, cornmeal and yeast food which was re-liquefied and supplemented with NR solution to a final concentration of 500 μM or an equivalent volume of vehicle (water). Climbing assay was performed as previously described (Greene et al., 2003). *Drosophila* brains were dissected from 30-day old flies and immunostained with anti-tyrosine hydroxylase. Brains were imaged with an

Olympus FV1000 confocal with SIM-scanner on a BX61 upright microscope using a 63X oil 0.95 NA objective. Tyrosine hydroxylase-positive neurons were counted under blinded conditions.

Statistical analysis

The Statistical Package GraphPad Prism version 7.0b (GraphPad Software, San Diego California USA) was used to analyze the data. Statistical testing involved two-sided Fisher's exact test, two-tailed Student's t-test, One-way Anova with Bonferroni's multiple comparison test, Kruskal-Wallis with Dunn's multiple comparisons test as appropriate. Experiments have been repeated independently (n=independent differentiation onsets) and each genotype has been analysed in technical duplicate or triplicate for each independent experiment (as indicated in the figure legend). Data from individual genotypes have been pooled for each experiment and the mean from independent differentiations has been calculated for data representation. Data are expressed as mean + SEM or SD as indicated.

Antibodies

Antibody	Host	Dilution	Use	Brand	Catalog Nr.
β-Actin	mouse	1:20000	WB	Sigma Aldrich	A5441
Cathepsin L	mouse	1:1000	WB	BD Bioscience	611084
Drp1	mouse	1:750	WB	Santa Cruz Biotechnology	sc-271583
eif2-alpha	rabbit	1:1000	WB	Cell Signaling	#9722
Fis1	rabbit	1:1000	WB	Alexis	ALX-210-907
GAPDH	mouse	1:20000	WB	Meridian Life Science	H86504M
GBA	mouse	1:500	WB	Abnova	H00002629-M01
GBA N17	goat	1:2000	WB	Santa Cruz Biotechnology	sc-30844
GRP78/BiP	rabbit	1:3000	WB	Sigma Aldrich	G9043
HSP90	rabbit	1:20000	WB	Enzo Life Sciences	ADI-SPA-836
KDEL	mouse	1:500	WB	Santa Cruz Biotechnology	sc-58774
Lamp1	mouse	1:40	ICC	DSHB	H4A3
Lamp1	mouse	1:50	FCM	DSHB	H4A3
LC3	rabbit	1:1000	WB	Cell Signalling	#2775
MAP2	chicken	1:3000	ICC	Abcam	ab5392
MFN1	mouse	1:1000	WB	Abcam	ab57602
NRK1	mouse	1:200	WB	Santa Cruz Biotechnology	sc-398852
Opa1	mouse	1:1000	WB	BD Bioscience	612606
PARP1	rabbit	1:4000	WB	Cell Signaling	#9542
PERK	rabbit	1:500	WB	Santa Cruz Biotechnology	sc-13073
Phospho-eif2-alpha	rabbit	1:1000	WB	Cell Signaling	#9721
Phospho-PERK	rabbit	1:500	WB	Santa Cruz Biotechnology	sc-32577
TOM20	rabbit	1:50	FCM	Santa Cruz Biotechnology	sc-11415
TOM20	rabbit	1:2000	ICC	Santa Cruz Biotechnology	sc-11415
TOM70	rabbit	1:8000	WB	ProteinTech	14528
Total OXPHOS human WB antibody cocktail	mouse	1:1000	WB	Abcam	ab110411
TUBB3	mouse	1:1000	ICC	Biolegend	801201
Tyrosine Hydroxylase	mouse	1:100	IHC	Immunostar Inc.	22491
Tyrosine Hydroxylase	rabbit	1:500	ICC	Pel-Freeze Biologicals	P40101-150
Vinculin	mouse	1:3000	WB	Sigma Aldrich	V9131

Supplemental References

BIELAWSKI, J., PIERCE, J. S., SNIDER, J., REMBIESA, B., SZULC, Z. M. & BIELAWSKA, A. 2009. Comprehensive quantitative analysis of bioactive sphingolipids by high-performance liquid chromatography-tandem mass spectrometry. *Methods Mol Biol,* 579**,** 443-67.

GREENE, J. C., WHITWORTH, A. J., KUO, I., ANDREWS, L. A., FEANY, M. B. & PALLANCK, L. J. 2003. Mitochondrial pathology and apoptotic muscle degeneration in Drosophila parkin mutants. *Proc Natl Acad Sci U S A,* 100**,** 4078-83.

HUNG, Y. P., ALBECK, J. G., TANTAMA, M. & YELLEN, G. 2011. Imaging cytosolic NADH-NAD(+) redox state with a genetically encoded fluorescent biosensor. *Cell Metab,* 14**,** 545-54.

HUNG, Y. P. & YELLEN, G. 2014. Live-cell imaging of cytosolic NADH-NAD+ redox state using a genetically encoded fluorescent biosensor. *Methods Mol Biol,* 1071**,** 83-95.

KEATINGE, M., BUI, H., MENKE, A., CHEN, Y. C., SOKOL, A. M., BAI, Q., ELLETT, F., DA COSTA, M., BURKE, D., GEGG, M., TROLLOPE, L., PAYNE, T., MCTIGHE, A., MORTIBOYS, H., DE JAGER, S., NUTHALL, H., KUO, M. S., FLEMING, A., SCHAPIRA, A. H., RENSHAW, S. A., HIGHLEY, J. R., CHACINSKA, A., PANULA, P., BURTON, E. A., O'NEILL, M. J. & BANDMANN, O. 2015. Glucocerebrosidase 1 deficient Danio rerio mirror key pathological aspects of human Gaucher disease and provide evidence of early microglial activation preceding alpha-synuclein-independent neuronal cell death. *Hum Mol Genet,* 24**,** 6640-52.

RAN, F. A., HSU, P. D., WRIGHT, J., AGARWALA, V., SCOTT, D. A. & ZHANG, F. 2013. Genome engineering using the CRISPR-Cas9 system. *Nat Protoc,* 8**,** 2281-308.

SANCHEZ-MARTINEZ, A., BEAVAN, M., GEGG, M. E., CHAU, K. Y., WHITWORTH, A. J. & SCHAPIRA, A. H. 2016. Parkinson disease-linked GBA mutation effects reversed by molecular chaperones in human cell and fly models. *Sci Rep,* 6**,** 31380.

SAWKAR, A. R., SCHMITZ, M., ZIMMER, K. P., RECZEK, D., EDMUNDS, T., BALCH, W. E. & KELLY, J. W. 2006. Chemical chaperones and permissive temperatures alter localization of Gaucher disease associated glucocerebrosidase variants. *ACS chemical biology,* 1**,** 235-51.

SPINAZZI, M., CASARIN, A., PERTEGATO, V., SALVIATI, L. & ANGELINI, C. 2012. Assessment of mitochondrial respiratory chain enzymatic activities on tissues and cultured cells. *Nat Protoc,* 7**,** 1235-46.

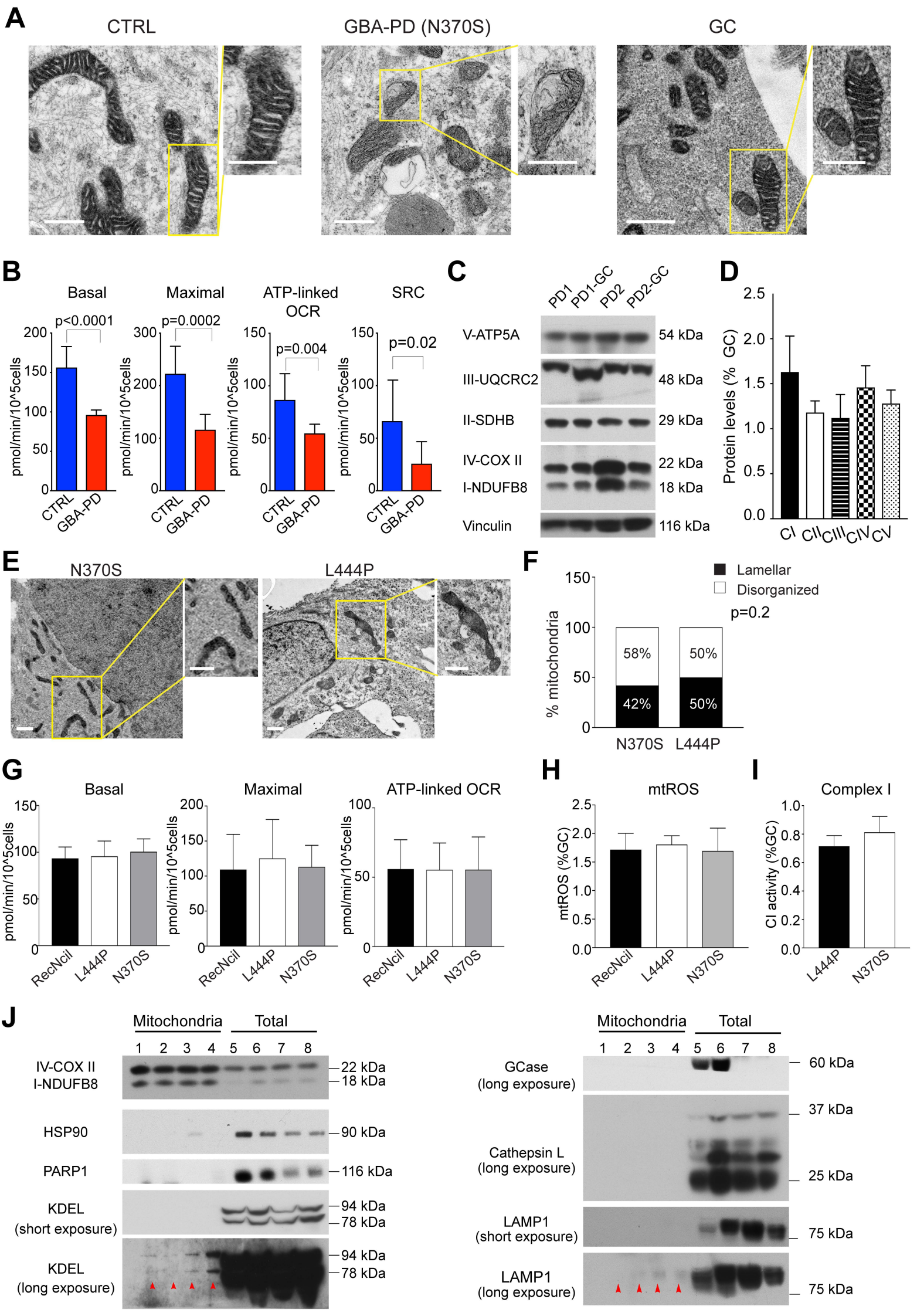
A
CTRL
GBA-PD (N370S)
GC
B
Basal
Maximal
ATP-linked OCR
SRC
p<0.0001
p=0.0002
p=0.004
p=0.02
pmol/min/10^5cells
CTRL
GBA-PD
C
PD1
PD1-GC
PD2
PD2-GC
V-ATP5A
III-UQCRC2
II-SDHB
IV-COX II
I-NDUFB8
Vinculin
54 kDa
48 kDa
29 kDa
22 kDa
18 kDa
116 kDa
D
Protein levels (% GC)
CI
CII
CIII
CIV
CV
E
N370S
L444P
F
Lamellar
Disorganized
p=0.2
% mitochondria
58%
42%
50%
50%
N370S
L444P
G
Basal
Maximal
ATP-linked OCR
pmol/min/10^5cells
RecNcil
L444P
N370S
H
mtROS
mtROS (%GC)
I
Complex I
CI activity (%GC)
J
Mitochondria
Total
1 2 3 4 5 6 7 8
IV-COX II
I-NDUFB8
22 kDa
18 kDa
HSP90
90 kDa
PARP1
116 kDa
KDEL
(short exposure)
94 kDa
78 kDa
KDEL
(long exposure)
94 kDa
78 kDa
GCase
(long exposure)
60 kDa
Cathepsin L
(long exposure)
37 kDa
25 kDa
LAMP1
(short exposure)
75 kDa
LAMP1
(long exposure)
75 kDa

Figure S1, related to Figure 1.

Mitochondrial function in *GBA*-PD iPSC-neurons. (A) TEM of mitochondrial morphology of healthy control (CTRL), *GBA*-PD (N370S) and gene corrected (GC) iPSC-derived neurons. Representative TEM images of mitochondria are shown (scale bar 500 nm). **(B)** Mitochondrial respiration in healthy control (CTRL) and *GBA*-PD (N370S, L444P, RecNcil) iPSC-derived neurons. Oxygen consumption rates (OCR) were measured over time after the sequential addition of oligomycin, CCCP and rotenone/antimycin A in iPSC-neurons. Values for basal OCR, ATP-linked OCR, maximal OCR, and spare respiratory capacity (SRC) are shown. Data are represented as mean + SD (n=5-7; two-tailed t-test). **(C, D)** Western blot analysis of the level of OXPHOS complexes in isogenic *GBA*-PD and GC iPSC-neurons. Representative blot is shown in (C) and the quantification is shown in (D). Data are represented as a fold ratio of *GBA*-PD to GC controls + SEM (n = 7). **(E)** Representative TEM images of mitochondrial morphology of *GBA*-PD (N370S and L444P) iPSC-neurons (scale bar 500 nm). **(F)** Quantification of mitochondrial cristae morphology in *GBA*-PD (N370S, L444P) iPSC-derived neurons (n=3; two-sided Fisher's exact test). **(G)** Mitochondrial respiration in *GBA*-PD (N370S, L444P, RecNcil) iPSC-derived neurons. Oxygen consumption rates (OCR) were measured over time after the sequential addition of oligomycin, CCCP and rotenone/antimycin A in iPSC-neurons. Values for basal, maximal, and ATP-linked OCR are shown. Data are represented as mean + SD (n=8; two-tailed t-test). **(H)** Mitochondrial ROS (mtROS) levels were determined by FACS using MitoSOX Red in *GBA*-PD (N370S, L444P, RecNcil) and GC controls iPSC-neurons. Data are normalized to GC and represented as mean + SEM (n=5; two-tailed t-test). **(I)** Enzymatic assays for complex (CI) activity from human mitochondrial extracts enriched from isogenic *GBA*-PD (N370S, L444P) and normalized to corresponding GC iPSC-neurons. Data are expressed as mean + SEM (n=5; two-tailed t-test). **(J)** Purification of mitochondria from iPSC-derived neurons. Validation of purity of mitochondria was performed by Western blot. Twenty micrograms of each sample (lanes 1-4: purified mitochondria; lanes 5-8: total cell lysate) from GC, *GBA*-PD, and two *GBA* KO lines were subjected to western blotting against mitochondrial complex proteins (IV-COX II, I-NDUFB8), cytosolic protein (HSP90), nuclear protein (PARP1), ER protein (KDEL), lysosomal proteins (GCase, Cathepsin L, LAMP1). Long exposures were used to detect contamination with non-mitochondrial proteins. Red arrows indicate the low amount of contamination with the ER and lysosomal proteins, KDEL and LAMP1.

A

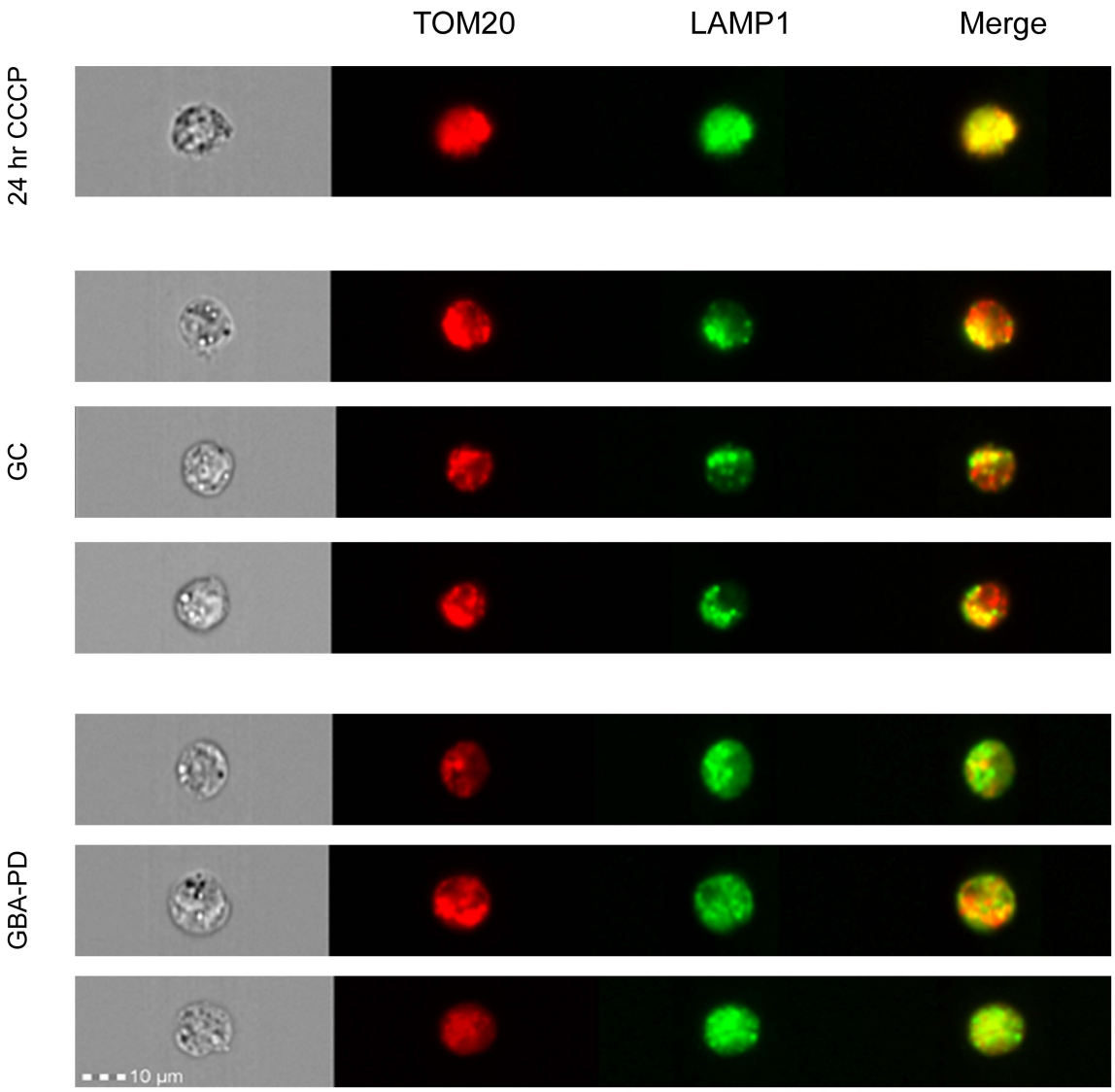
TOM20
LAMP1
Merge
24 hr CCCP
GC
GBA-PD
10 µm

B

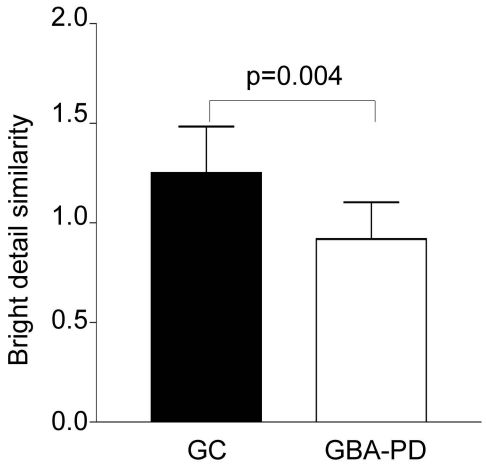
2.0
1.5
1.0
0.5
0.0
p=0.004
Bright detail similarity
GC
GBA-PD

Figure S2, related to Figure 2.

ImageStream analysis of lysosomal/mitochondrial colocalization. (A) Representative ImageStream images showing TOM20/LAMP1 in *GBA*-PD iPSC-neurons and corresponding isogenic controls. Cells treated with 10 μM CCCP for 24 hours were used as positive control. **(B)** Bright detail similarity (BDS) score is indicated as quantification. Data are represented as mean + SD (n=4, two-tailed t-test). BDS for CCCP-treated samples, mean=2.1±0.2.

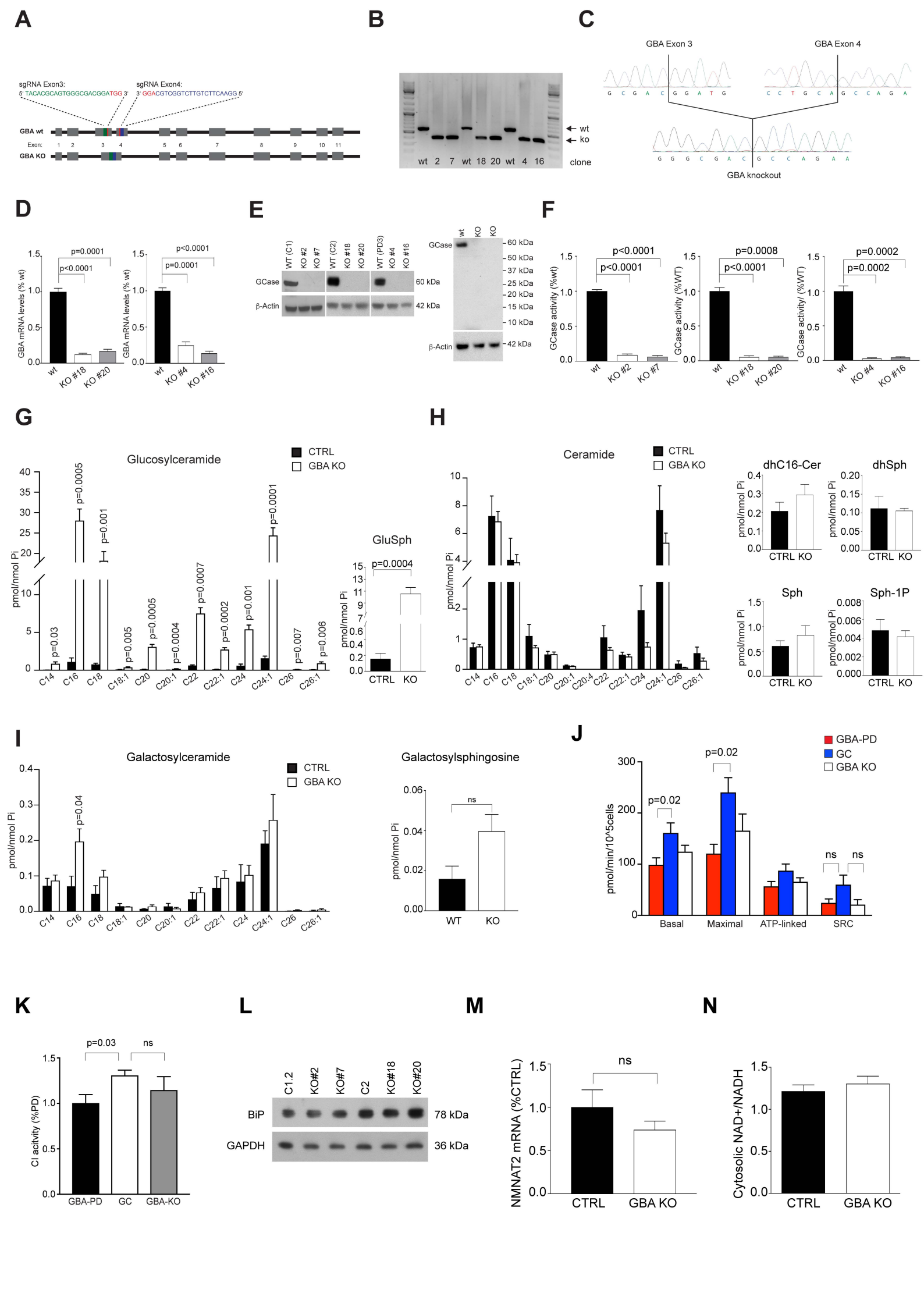
A
sgRNA Exon3:
5' TACACGCAGTGGGCGACGGATGG 3'
sgRNA Exon4:
3' GGACGTCGGTCTTGTCTTCAAGG 5'
GBA wt
Exon: 1 2 3 4 5 6 7 8 9 10 11
GBA KO
B
wt
ko
wt 2 7 wt 18 20 wt 4 16
clone
C
GBA Exon 3
GBA Exon 4
GBA knockout
D
GBA mRNA levels (% wt)
p=0.0001
p<0.0001
p<0.0001
p=0.0001
wt
KO #18
KO #20
KO #4
KO #16
E
WT (C1)
KO #2
KO #7
WT (C2)
KO #18
KO #20
WT (PD3)
KO #4
KO #16
GCase
β-Actin
60 kDa
42 kDa
wt
KO
KO
60 kDa
50 kDa
37 kDa
25 kDa
20 kDa
15 kDa
10 kDa
42 kDa
F
GCase activity (%wt)
GCase activity (%WT)
GCase activity/ (%WT)
p<0.0001
p<0.0001
p=0.0008
p<0.0001
p=0.0002
p=0.0002
wt
KO #2
KO #7
KO #18
KO #20
KO #4
KO #16
G
Glucosylceramide
CTRL
GBA KO
pmol/nmol Pi
p=0.03
p=0.005
p=0.0005
p=0.0004
p=0.0007
p=0.0002
p=0.001
p=0.0001
p=0.007
p=0.006
p=0.0005
p=0.001
C14 C16 C18 C18:1 C20 C20:1 C22 C22:1 C24 C24:1 C26 C26:1
GluSph
p=0.0004
CTRL KO
H
Ceramide
CTRL
GBA KO
pmol/nmol Pi
C14 C16 C18 C18:1 C20 C20:1 C20:4 C22 C22:1 C24 C24:1 C26 C26:1
dhC16-Cer
dhSph
Sph
Sph-1P
pmol/nmol Pi
CTRL KO
I
Galactosylceramide
CTRL
GBA KO
pmol/nmol Pi
p=0.04
C14 C16 C18 C18:1 C20 C20:1 C22 C22:1 C24 C24:1 C26 C26:1
Galactosylsphingosine
pmol/nmol Pi
ns
WT KO
J
GBA-PD
GC
GBA KO
pmol/min/10^5cells
p=0.02
p=0.02
ns
ns
Basal
Maximal
ATP-linked
SRC
K
CI activity (%PD)
p=0.03
ns
GBA-PD
GC
GBA-KO
L
C1.2
KO#2
KO#7
C2
KO#18
KO#20
BiP
GAPDH
78 kDa
36 kDa
M
NMNAT2 mRNA (%CTRL)
ns
CTRL
GBA KO
N
Cytosolic NAD+/NADH
CTRL
GBA KO

Figure S3, related to Figure 3 and Figure 4.

Mitochondrial function in *GBA* knockout (KO) human iPSC-derived neurons. (A) Schematic diagram showing the wild-type (wt) *GBA* gene and the targeting strategy for the generation of *GBA* KO human iPSCs. Two single guide RNAs (sgRNAs) were designed to introduce DNA double-strand breaks in exon 3 and 4 in the *GBA* gene resulting in a shift of open reading frame and consequently an early stop codon. Grey boxes represent exons and blue and green areas binding sequences of the corresponding sgRNA. **(B)** Genomic cleavage analysis of the *GBA* locus by PCR and agarose gel electrophoresis. **(C)** Schematic representation of the genomic deletion at the *GBA* locus showing gene sequence of wt *GBA* gene (exon 3 and exon 4, upper lane) and the *GBA* knockout (*GBA* KO) allele (bottom lane) after successful double-strand DNA cleavage with the CRISPR-Cas9 system. **(D)** *GBA* mRNA levels in control iPSCs (line C2) and *GBA*-PD (line PD3) iPSC-derived neurons and corresponding isogenic *GBA* KO clones (C2, clones #18 and #20; PD3, clones #4 and #16, respectively). Data are normalized on Rplp0 and represented as mean + SEM (n=3; two-tailed t-test). **(E)** Left panel, representative Western blots showing the absence of GCase in individual clones of *GBA* KO neurons derived from two independent control human iPSC lines (C1.2, knockout clones #2 and #7; C2, knockout clones #18 and #20) or *GBA*-PD iPSCs with N370S *GBA* mutation (PD3, knockout clones #4 and #16). Right panel, representative Western blot with an antibody targeting the N-terminus of GCase (N17) showing the absence of truncated protein in *GBA* KO iPSC-derived neurons. **(F)** GCase activity in *GBA* KO and isogenic control iPSC-neurons. Data are represented as mean + SEM (n=3; two-tailed t-test). **(G-I)** HPLC-MS/MS measurement of total sphingolipids in CTRL and *GBA* KO iPSC-derived neurons. (G) Glucosylceramide species and glucosylsphingosine. (H) Ceramide species, dhC16-Cer, dhSphingosine, sphingosine, and sphingosine 1-phosphate. (I) Galactosylceramide species and galactosylsphingosine. Data are normalized to inorganic phosphate (Pi) and represented as mean + SEM (n=4; two-tailed t-test). **(J)** Mitochondrial respiration in isogenic *GBA*-PD (N370S), gene corrected (GC) controls and *GBA* KO iPSC-derived neurons. Oxygen consumption rates (OCR) were measured over time after the sequential addition of oligomycin, CCCP and rotenone/antimycin A in iPSC-neurons. Values for basal OCR, ATP-linked OCR, maximal OCR, and spare respiratory capacity (SRC) are shown. Data are represented as mean + SD (n=5-7; one-way ANOVA). **(K)** Complex I (CI) activity was assessed in mitochondrial extracts from isogenic *GBA*-PD, GC and *GBA* KO iPSC-neurons. Data are represented as mean + SEM (n=5; one-way ANOVA). **(L)** Western blot depicting the ER stress related protein BiP in *GBA* KO iPSC-derived neurons and corresponding isogenic controls. **(M)** NMNAT2 mRNA levels in isogenic CTRL and *GBA* KO iPSC-neurons. Data are normalized to the level of the housekeeping genes Rplp0 and OAZ and expressed as fold change over CTRL. Data are expressed as mean + SEM (n=5; two-tailed t-test). **(N)** The NAD+/NADH redox state was measured in CTRL and *GBA* KO iPSC-derived DA neurons using the biosensor Peredox. Results are presented as mean + SEM (n=5; two-tailed t-test).

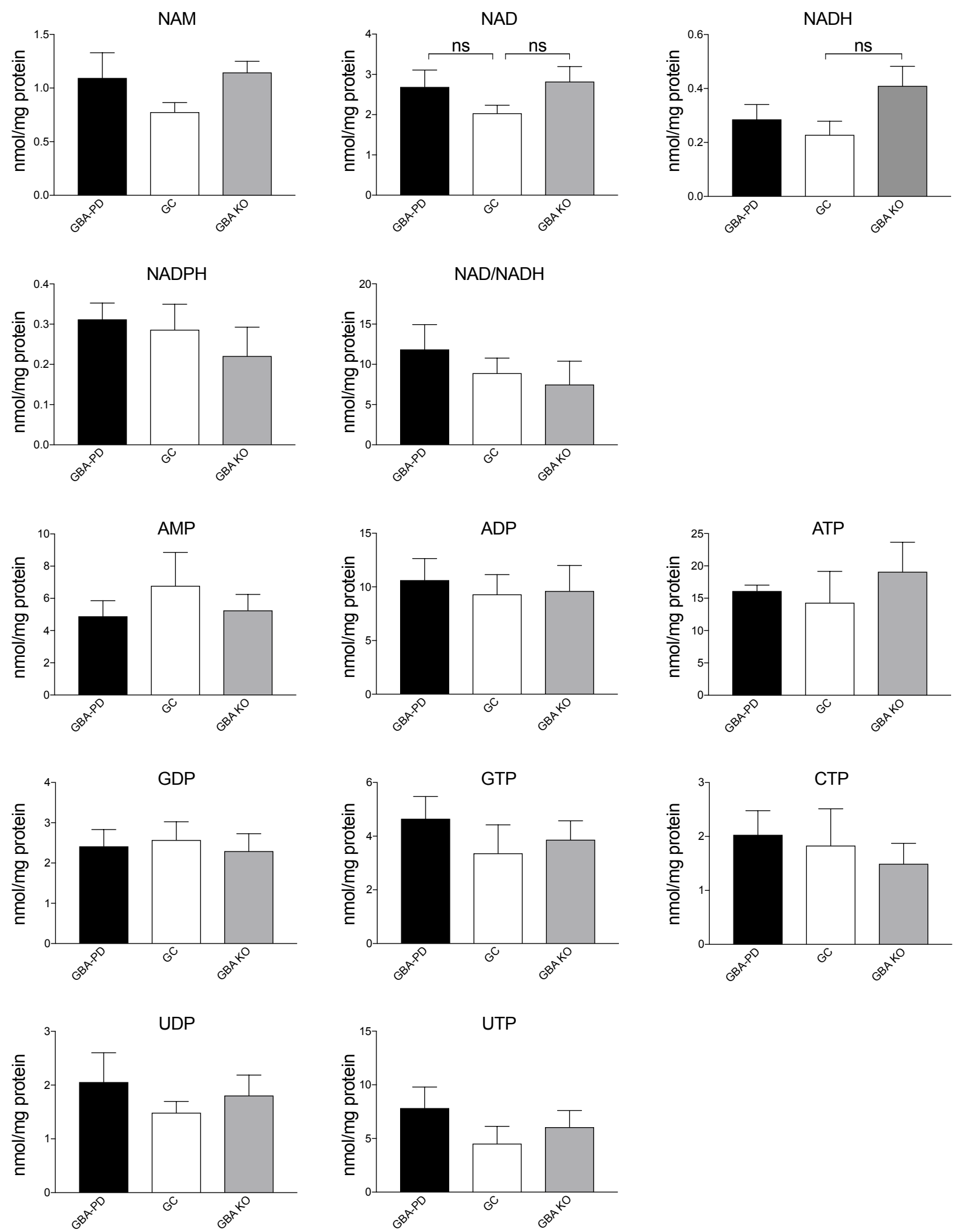
NAM
nmol/mg protein
1.5
1.0
0.5
0.0
GBA-PD
GC
GBA KO
NAD
ns
ns
4
3
2
1
0
NADH
ns
0.6
0.4
0.2
0.0
NADPH
0.4
0.3
0.2
0.1
0.0
NAD/NADH
20
15
10
5
0
AMP
10
8
6
4
2
0
ADP
15
10
5
0
ATP
25
20
15
10
5
0
GDP
4
3
2
1
0
GTP
6
4
2
0
CTP
3
2
1
0
UDP
3
2
1
0
UTP
15
10
5
0

Figure S4, related to Figure 5.

LC/MS-based targeted metabolomics in *GBA*-PD, isogenic control and *GBA* KO iPSC-derived neurons. *GBA*-PD (N370S, L444P), isogenic GC and *GBA* KO (clones #4 and #16) iPSCs were differentiated into DA neurons for 55 days and pyridine and adenine nucleotides were measured using HPLC coupled to mass spectrometry. Data are expressed as mean + SEM (*GBA*-PD and GC n= 5-7; *GBA* KO, n=4).

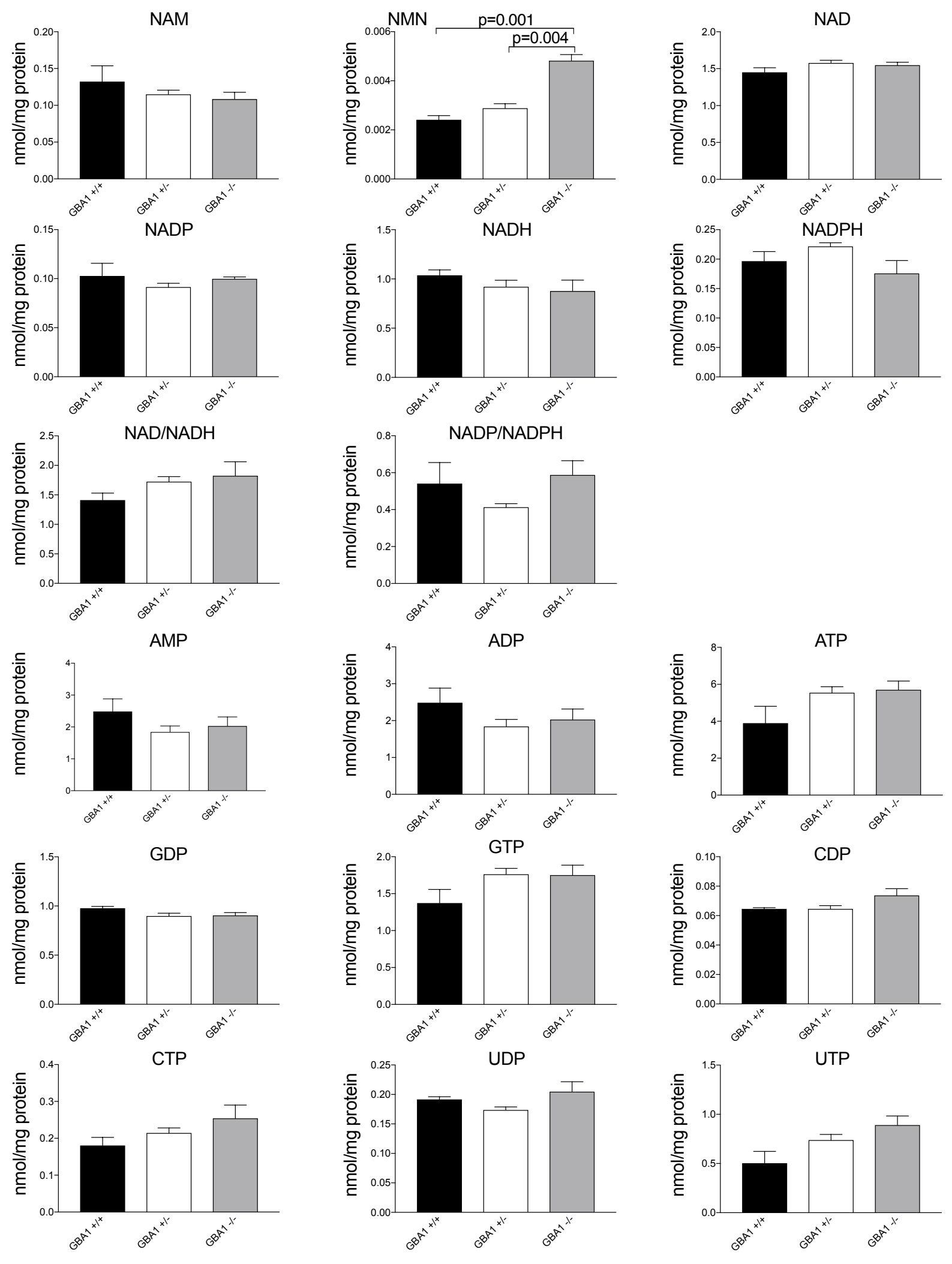
NAM
NMN
p=0.001
p=0.004
NAD
NADP
NADH
NADPH
NAD/NADH
NADP/NADPH
AMP
ADP
ATP
GDP
GTP
CDP
CTP
UDP
UTP
nmol/mg protein
GBA1 +/+
GBA1 +/-
GBA1 -/-

Figure S5, related to Figure 5.

LC/MS-based targeted metabolomics in zebrafish brains. Pyridine and adenine nucleotides were measured using HPLC coupled to mass spectrometry in brains of 2-month old *gba*$^{+/+}$, *gba*$^{+/-}$ and *gba*$^{-/-}$ zebrafish. Data are expressed as mean + SEM (n=3; two-tailed t-test).

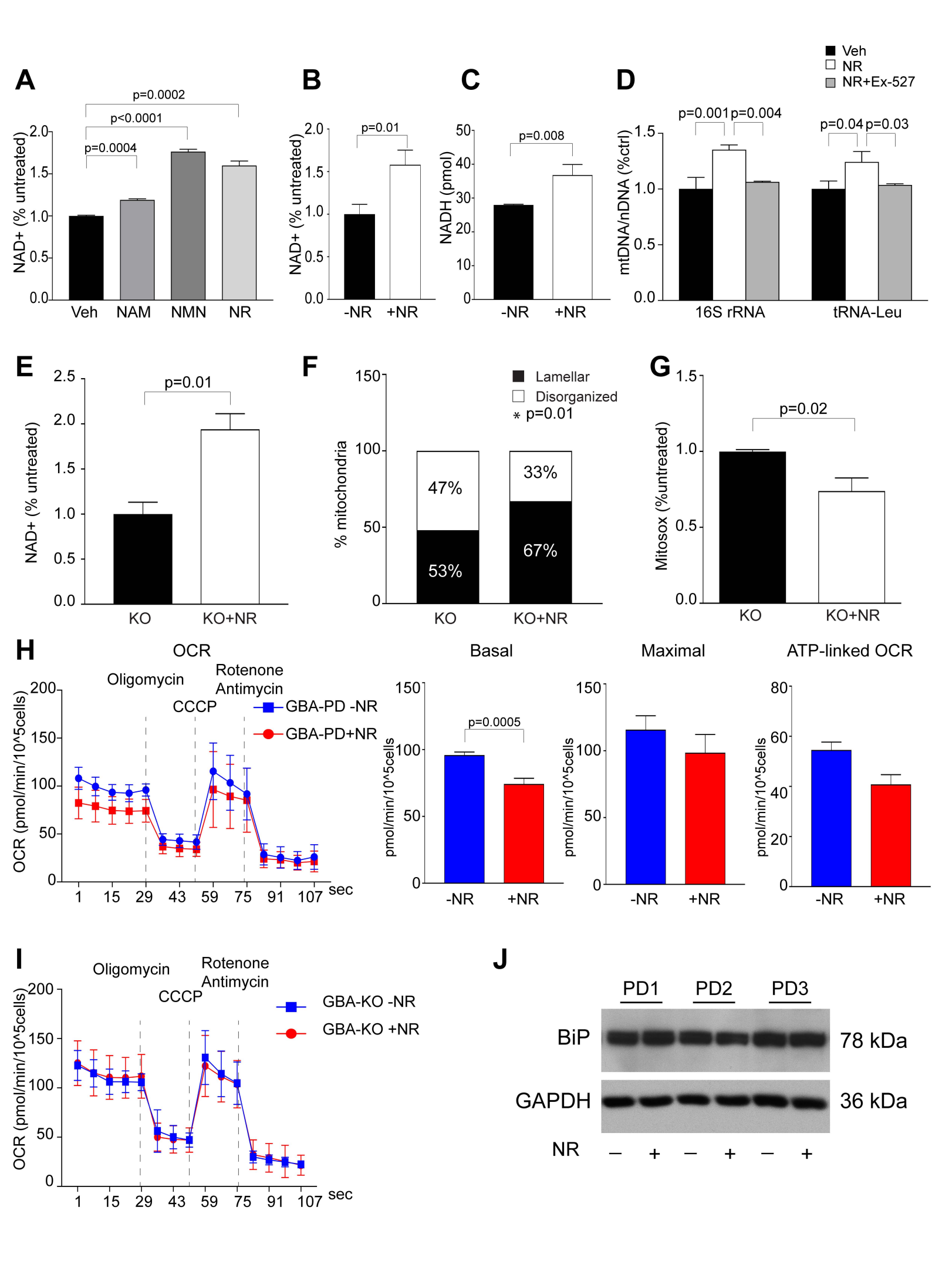
A
p=0.0002
p<0.0001
p=0.0004
NAD+ (% untreated)
Veh
NAM
NMN
NR
B
p=0.01
NAD+ (% untreated)
-NR
+NR
C
p=0.008
NADH (pmol)
-NR
+NR
D
Veh
NR
NR+Ex-527
p=0.001
p=0.004
p=0.04
p=0.03
mtDNA/nDNA (%ctrl)
16S rRNA
tRNA-Leu
E
p=0.01
NAD+ (% untreated)
KO
KO+NR
F
Lamellar
Disorganized
* p=0.01
% mitochondria
47%
53%
33%
67%
KO
KO+NR
G
p=0.02
Mitosox (%untreated)
KO
KO+NR
H
OCR
Oligomycin
Rotenone
Antimycin
CCCP
GBA-PD -NR
GBA-PD+NR
OCR (pmol/min/10^5cells)
sec
Basal
Maximal
ATP-linked OCR
p=0.0005
pmol/min/10^5cells
-NR
+NR
I
Oligomycin
Rotenone
Antimycin
CCCP
GBA-KO -NR
GBA-KO +NR
OCR (pmol/min/10^5cells)
sec
J
PD1
PD2
PD3
BiP
78 kDa
GAPDH
36 kDa
NR
– + – + – +

Figure S6, related to Figure 5.

Nicotinamide riboside treatment in *GBA*-PD and *GBA* KO iPSC-neurons. (A) Control iPSC-derived neurons were treated with 0.5 mM nicotinamide (NAM), 0.5 mM nicotinamide mononucleotide (NMN), 0.5 mM nicotinamide riboside (NR) or vehicle (Veh) and NAD+ levels were measured using a NAD+ cycling assay. Results are normalized to vehicle-treated and represented as mean + SEM (n=3; two-tailed t-test compared to vehicle-treated). **(B)** *GBA*-PD iPSC-derived neurons were treated with NR and NAD+ levels were measured using a NAD+ cycling assay. Results are normalized to untreated and represented as mean + SEM (n=3; two-tailed t-test). **(C)** iPSC-derived neurons were treated with NR and NADH levels were measured with a NAD+ cycling assay. Results are normalized to untreated and represented as mean + SEM (n=3; two-tailed t-test compared to untreated). **(D)** *GBA*-PD iPSC-derived neurons were treated with NR plus 100 nM EX-527 for 24 hours and mtDNA content was assessed by qRT-PCR as mitochondrial (16S rRNA and tRNA-Leu) to nuclear (ß-2M) DNA ratio. Data are normalized to untreated and expressed as mean + SEM (n=5; two-tailed t-test). **(E)** *GBA* KO iPSC-derived neurons were treated with NR and NAD+ levels were measured using a NAD+ cycling assay. Results are normalized to untreated and represented as mean + SEM (n=3; two-tailed t-test compared to untreated). **(F)** NR treatment rescues mitochondrial morphological alterations in *GBA* KO iPSC-derived neurons. *GBA* KO iPSC-derived neurons (clones #2, #7 and clones #18, #20) were treated with NR and mitochondrial morphology was assessed by TEM. Mitochondria were counted from at least 50 individual cells and scored for normal (lamellar) or ballooned/swollen cristae (disorganized) (n=3; two-sided Fisher's exact test). **(G)** NR treatment reduces mtROS production in *GBA* KO neurons. *GBA* KO iPSC-derived neurons were treated with NR and mtROS levels were determined with MitoSOX Red using FACS. Data are normalized to the corresponding untreated control and represented as mean + SEM (n=5; two-tailed t-test). **(H)** Mitochondrial respiration in NR-treated *GBA*-PD iPSC-neurons. Values for basal OCR, ATP-linked OCR, and maximal OCR, are shown. Data are represented as mean + SD (n=8; two-tailed t-test). **(I)** Mitochondrial respiration in NR-treated *GBA* KO iPSC-neurons. Values for basal OCR, ATP-linked OCR, and maximal OCR are shown. Data are represented as mean + SD (n=8; two-tailed t-test). **(J)** *GBA*-PD neurons were treated with NR and levels of BiP were assessed by Western blot.

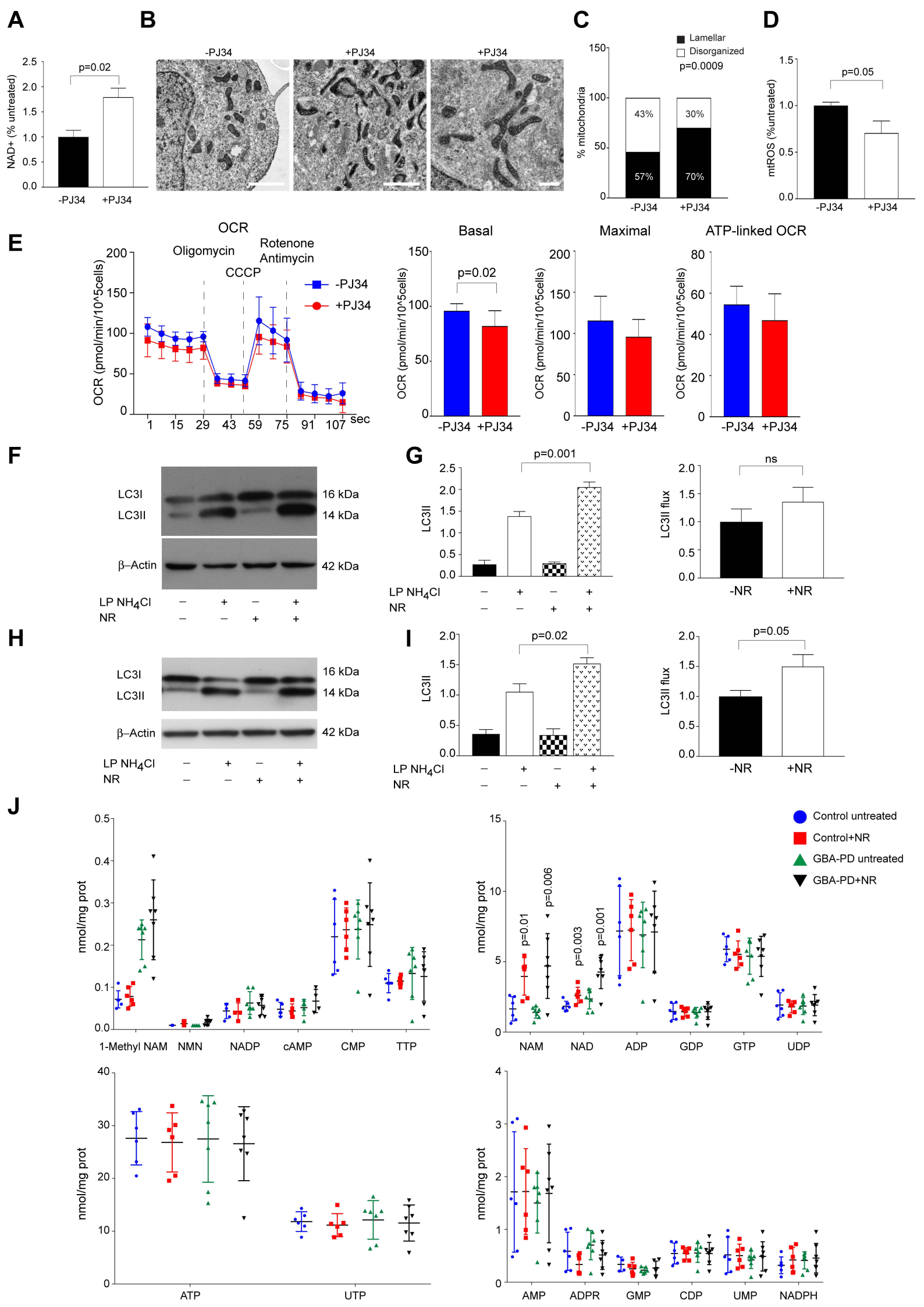
A
NAD+ (% untreated)
p=0.02
-PJ34
+PJ34
B
-PJ34
+PJ34
+PJ34
C
Lamellar
Disorganized
p=0.0009
% mitochondria
43%
57%
30%
70%
-PJ34
+PJ34
D
mtROS (%untreated)
p=0.05
-PJ34
+PJ34
E
OCR
Oligomycin
Rotenone
Antimycin
CCCP
-PJ34
+PJ34
OCR (pmol/min/10^5cells)
sec
Basal
Maximal
ATP-linked OCR
p=0.02
F
LC3I
LC3II
β–Actin
16 kDa
14 kDa
42 kDa
LP NH4Cl
NR
G
LC3II
p=0.001
LC3II flux
ns
-NR
+NR
H
I
p=0.02
p=0.05
J
Control untreated
Control+NR
GBA-PD untreated
GBA-PD+NR
nmol/mg prot
1-Methyl NAM
NMN
NADP
cAMP
CMP
TTP
NAM
NAD
ADP
GDP
GTP
UDP
p=0.01
p=0.006
p=0.003
p=0.001
ATP
UTP
AMP
ADPR
GMP
CDP
UMP
NADPH

Figure S7, related to Figure 6.

NAD+ boosting treatments in *GBA*-PD iPSC-neurons.

(A) Control iPSC-derived neurons were treated with PJ34 and NAD+ levels were measured using a NAD+ cycling assay. Data are normalized to untreated and expressed as mean + SEM (n=5; two-tailed t-test). **(B)** Representative TEM images showing *GBA*-PD iPSC-neurons with or without PJ34 treatment (scale bar 500 nm). **(C)** Quantification of mitochondrial cristae morphology in PJ34 treated and untreated *GBA*-PD iPSC-neurons (n=3; two-sided Fisher's exact test). **(D)** mtROS in *GBA*-PD (N370S, L444P) iPSC-neurons after PJ34 treatment. Data are normalized to the corresponding untreated control and represented as mean + SEM (n=3; two-tailed t-test). **(E)** Mitochondrial respiration in PJ34-treated *GBA*-PD (N370S, L444P) iPSC-neurons. Values for basal OCR, ATP-linked OCR, and maximal OCR, are shown. Data are represented as mean + SD (n=5-7; two-tailed t-test). **(F)** *GBA*-PD iPSC-neurons were treated with NR (+) or vehicle (-) and Western blot analysis for LC3 was performed in iPSC-neurons, untreated (−) or treated (+) with 200 µM leupeptin (LP) and 20 mM NH_4Cl for 4 hrs. A representative Western blot is shown. **(G)** Quantification of levels of LC3-II (left) and LC3 flux (right). Intensities of Western blot bands were normalized to β-Actin. LC3 flux data are normalized to untreated. Data are represented as mean + SEM (n=5; two-tailed t-test). **(H)** *GBA* KO iPSC-neurons were treated with NR or vehicle and Western blot analysis for LC3 was performed in iPSC-neurons, untreated (−) or treated (+) with 200 µM leupeptin (LP) and 20 mM NH_4Cl for 4 hrs. A representative Western blot is shown. **(I)** Quantification of levels of LC3-II (left) and LC3-II flux (right). Intensities of Western blot bands were normalized to β-Actin. LC3 flux data are normalized to untreated. Data are represented as mean + SEM (n=5; two-tailed t-test). **(J)** LC/MS-based targeted metabolomics in iPSC-derived neurons treated with NR. Control and *GBA*-PD (N370S) iPSC-neurons were treated with 0.5 mM NR for 24 hours and LC/MS-based targeted NAD+ metabolomics was performed. Data are normalized on protein concentration and represented as mean ± SD (n=7 independent differentiations; two-tailed t-test treated vs untreated).

Table S1, related to Figure 1-6 and Figure S1-S7.
List of *GBA*-PD iPSC lines used in the study.

iPSC clone ID	Diagnosis	Genotype	Genome editing
C1.1	HC	wt/wt	
C1.2	HC	wt/wt	
C2	HC	wt/wt	
PD1	PD	RecNcil/wt	
PD1 GC	PD	wt/wt	Gene corrected line
PD2	PD	L444P/wt	
PD2 GC	PD	wt/wt	Gene corrected line
PD2-1	PD	L444P/wt	
PD3	PD	N370S/wt	
PD3 GC	PD	wt/wt	Gene corrected line
PD4	PD	N370S/wt	

HC, healthy control; PD, Parkinson's disease; GC, gene corrected.

Table S2, related to Figure S3.
List of *GBA* knockout human iPSC lines generated and used in the study.

Parental iPSC line	Parental GBA genotype	Derived iPSC clones	Derived GBA genotype
C1.2	wt/wt	GBA KO # 2 and #7	-/-
C2	wt/wt	GBA KO #18 and #20	-/-
PD3	N370S/wt	GBA KO #4 and #16	-/-

***GBA* knockout iPSC lines generated and used in the study.** Table showing the list of *GBA* knockout iPSC lines generated using CRISPR-Cas9. HC, healthy control; PD, Parkinson's disease.

INVENTORY OF SUPPLEMENTAL INFORMATION

Supplementary Experimental Procedures

Detailed description of the experimental procedures and source of materials.

Figure S1

Supporting data for Figure 1.

Figure S2

Supporting data for Figure 2.

Figure S3

Supporting data for Figure 3 and Figure 4.

Figure S4

Supporting data for Figure 5.

Figure S5

Supporting data for Figure 5.

Figure S6

Supporting data for Figure 5.

Figure S7

Supporting data for Figure 6.

Table S1

List of cell lines used in the study.

Table S2

List of GBA knockout human iPSC lines generated and used in the study.